Separation Delay in Turbulent Boundary Layers via Model Predictive Control of Large-Scale Motions

Alexandros Tsolovikos,[a] Akshit Jariwala,[a] Saikishan Suryanarayanan,[b] Efstathios Bakolas,[a] and David Goldstein[a]

(Dated: 24 September 2023)

Turbulent boundary layers are dominated by large-scale motions (LSMs) of streamwise momentum surplus and deficit that contribute significantly to the statistics of the flow. In particular, the high-momentum LSMs residing in the outer region of the boundary layer have the potential to re-energize the flow and delay separation if brought closer to the wall. This work explores the effect of selectively manipulating LSMs in a moderate Reynolds number turbulent boundary layer for separation delay via well-resolved large-eddy simulations. Toward that goal, a model predictive control scheme is developed based on a reduced-order model of the flow that directs LSMs of interest closer to the wall in an optimal way via a body force-induced downwash. The performance improvement achieved by targeting LSMs for separation delay, compared to a naive actuation scheme that does not account for the presence of LSMs, is demonstrated.

I. INTRODUCTION

Studies on the structure of wall-bounded turbulent flows have led to the observation of large-scale and very-large-scale motions (LSMs/VLSMs) that exhibit long temporal and spatial coherence of the streamwise velocity fluctuations in the order of the boundary layer thickness. These large coherent structures are commonly found in the log and outer region of zero pressure gradient (ZPG) turbulent boundary layers (TBLs)[1–5], as well as pipe[6,7] and channel flows[8,9] and are typically formed by the coherent alignment of hairpin vortices in the streamwise direction into groups of hairpins[10].

These LSMs are typically encountered as regions of momentum deficit, surrounded by regions of momentum surplus, extending a few times the boundary layer thickness δ in the streamwise direction. The fast and slow LSMs are critical in producing and transporting turbulent kinetic energy and contribute significantly to the Reynolds shear stresses.

In TBLs subject to adverse pressure gradients (APG), which are often encountered in real engineering applications, such as airfoils, turbine blades, and diffusers, the prevailing contribution of LSMs on the flow statistics has also been reported[11–14]. Studies have found that the length of LSMs tends to increase with increasing APG up until a point where a continuing increase of APG suppresses the formation of hairpin packets, leading to a decrease in the streamwise but an increase in the spanwise coherence of LSMs[15].

Considering the significant role that LSMs play in turbulent flows, the present study proposes a novel flow control strategy in which separation delay is achieved by manipulating naturally occurring LSMs in a turbulent boundary layer. While previous studies have attempted to manipulate both near-wall structures[16–19] and LSMs in the logarithmic region[20,21] for drag reduction, the potential of targeting LSMs – especially the high-momentum LSMs – for separation delay has only recently been explored[22,23]. Increasing the near-wall momentum just before the separation point can be beneficial to delaying or preventing separation, and selectively directing these high-momentum LSMs toward the wall has the potential to increase wall shear stress, as well as mixing near the wall[22,24]. The present study aims to manipulate high-momentum LSMs in an APG TBL by bringing them closer to the wall to re-energize the near-wall boundary layer and prevent separation. This is in contrast to recent separation delay studies using, for instance, synthetic jet actuators[25] and dielectric barrier discharge actuators[26] that do not account for the presence of LSMs in the flow.

Such an active control scheme requires 1) detecting the LSMs of interest (e.g., using wall shear stress or pressure measurements[27–29]) and 2) deciding *whether* and *when* to actuate on the oncoming LSMs.

The present work is the first numerical study that explores the effect that manipulating LSMs has on separation delay in an adverse pressure gradient turbulent boundary layer. It employs well-resolved large-eddy simulations (LES) of a moderate Reynolds number APG TBL of $Re_\theta = 1551$ based on the momentum thickness θ at the inlet. Actuation is performed using a near-wall jet modeled as a body force field with a Gamma distribution in the streamwise direction and a Gaussian distribution in the wall-normal and spanwise directions, inspired by the effect that dielectric barrier plasma actuators[30] and jet-assisted surface mounted actuators[31] have on entraining flow toward the wall. In the interest of simplicity, the LSMs are detected upstream of the actuator via box-filtering of the 3-dimensional streamwise velocity fluctuations within an off-wall *observation grid*. That is, in the present work, the more difficult problem of detecting low/high-momentum LSMs using wall measurements, such as in Refs. 27–29, is sidestepped.

The decision of whether to actuate on an oncoming LSM is made via a *model predictive control* (MPC) policy that: 1) predicts how an LSM that has been detected upstream will move downstream toward the actuator using *Taylor's hypothesis*[1,32–34] and 2) solves an optimal output tracking control problem for a binary on/off input to the actuator that maximizes the downwash experienced by an LSM of interest (here, fast-moving LSMs) while avoiding the opposite (i.e., low-momentum) LSMs and minimizing actuation cost. Since this

[a]Department of Aerospace Engineering and Engineering Mechanics, The University of Texas at Austin
[b]Department of Mechanical Engineering, The University of Akron

is a model-based control scheme, the wall-normal velocity field that the jet creates is modeled using *total least squares dynamic mode decomposition*[35], extended here to systems with control inputs. This is in contrast to Ref. 21, where a wall-normal jet operated by a heuristics-based control policy was used to push fast-moving LSMs *away* from the wall with the goal of reducing drag in an experimental ZPG TBL.

The choice to selectively target high-speed LSMs for increasing near-wall momentum instead of utilizing blind actuation schemes, such as periodic blowing, is driven by two key factors. First, there is a need for an optimal control scheme that conserves energy by operating only when required. Second, a blind actuation scheme would bring both high and low-momentum LSMs toward the wall, which could contribute adversely to the desired momentum increase. The proposed control scheme not only re-energizes the flow near the wall with the momentum introduced by the actuator but also "reaps the whirlwind" of high-momentum LSMs that exist in the outer regions of the boundary layer, therefore supplementing the effect that a potentially weak actuator has on the flow.

The proposed actuation scheme is evaluated on its ability to increase near-wall momentum downstream of the actuator and at locations on the verge of or actually experiencing separation. For the APG LES, the prescribed wall-normal velocity at the top of the domain follows a blowing-suction profile that leads to an adverse-to-favorable pressure gradient and creates a separation bubble. The control scheme is extensively tested for its effectiveness in reducing the size of the separation bubble and delaying separation. The evaluation primarily focuses on the advantage of targeting high-momentum LSMs and pushing them toward the wall, compared to targeting low-momentum LSMs or employing random or continuous actuation strategies.

The paper is structured as follows: Section II presents the computational setup for the large-eddy simulation of a turbulent boundary layer with a separation bubble, as well as the actuator model. Section III details the proposed model predictive control scheme for targeting LSMs. Section IV showcases a series of numerical experiments that highlight the effectiveness of the proposed control scheme. Finally, conclusions and potential future directions for this work are discussed in Section V.

TABLE I: Nomenclature.

Symbol	Description
U_∞	free-stream velocity
δ_{in}	99% boundary layer thickness at the inlet
θ	momentum thickness
$(\cdot)_1$	quantity in the streamwise direction
$(\cdot)_2$	quantity in the wall-normal direction
$(\cdot)_3$	quantity in the spanwise direction
x_i	coordinate in the i-th direction
L_i	length of computational domain in the i-th direction
N_i	number of elements in the i-th direction
u_i	velocity in the i-th direction
u_i'	velocity fluctuation in the i-th direction
$\tilde{u}_i'$	filtered velocity fluctuation in the i-th direction
u_τ	friction velocity
ν	kinematic viscosity
V_{bleed}	constant wall-normal velocity at the top of the domain
$V_{top}(x_1)$	wall-normal velocity at the top of the domain and at x_1
x_b	center of the V_{top} velocity profile
σ_b	standard deviation of the V_{top} velocity profile
$\mathbf{e}_\phi$	direction of the jet force field
$\mathbf{f}$	jet body force field
$\tilde{g}(\cdot)$	spatial distribution of jet force field
G	jet power input
$x_{i,J}$	center of the jet force field distribution in the i-th direction
$\sigma_{i,J}$	standard deviation of the jet force field in the i-th direction
ϕ	pitch angle of the jet force field
$p(t)$	control input at time step t
$\mathbf{y}(t)$	u_2' at the control grid at time step t (vectorized)
$\mathbf{z}(t)$	reduced-order state at time step t
m	number of snapshots
n_p	number of control inputs
n_y	number of control grid points
n_z	number of reduced-order model states
dt	LES timestep
N_{mpc}	MPC horizon in number of ROM timesteps
N_{meas}	LSM measurement frequency, in number of ROM timesteps
T_{rom}	number of LES timesteps corresponding to one ROM timestep
$\mathbf{y}_{des}(t)$	desired u_2' at the control grid at time step t (vectorized)
π_t^*	optimal control policy computed at time step t

II. NUMERICAL SETUP

A. Large-Eddy Simulations

This study employs well-resolved large-eddy simulations (LES) of the turbulent flow over a flat plate. The incompressible Navier-Stokes and continuity equations

$$\frac{\partial \mathbf{u}}{\partial t} + (\mathbf{u}\cdot\nabla)\mathbf{u} = -\nabla p + \frac{1}{Re_{\delta_{\text{in}}}}\nabla\cdot(\nabla\mathbf{u}) + \mathbf{f} \tag{1}$$

$$\nabla\cdot\mathbf{u} = 0 \tag{2}$$

are non-dimensionalized by the free-stream velocity, U_∞, and the nominal 99% boundary layer thickness δ_{in} at the inlet. The position $\mathbf{x} = [x_1,\ x_2,\ x_3]$ and velocity $\mathbf{u} = [u_1,\ u_2,\ u_3]$ vectors consist of their streamwise, wall-normal, and spanwise components, respectively. The Reynolds number based on δ_{in} is $Re_{\delta_{\text{in}}} = 13191$ and corresponds to a momentum thickness θ-based Reynolds number of $Re_\theta = 1551$. In addition, the acceleration term $\mathbf{f}$ is included and subsequently used to model the desired behavior of the actuator.

The streamwise length of the domain is $L_1 = 80\delta_{\text{in}}$, the height is $L_2 = 10\delta_{\text{in}}$ and the spanwise extent is $L_3 = 8\delta_{\text{in}}$. The governing equations are solved using the high-order spectral element solver Nek5000[36,37]. The domain is decomposed into $N_1 = 260$, $N_2 = 26$, and $N_3 = 40$ elements in the streamwise, wall-normal, and spanwise directions. Within each element, both the velocity and pressure fields are expressed as Legendre polynomials of order $N = 7$ ($\mathbb{P}_N - \mathbb{P}_N$ formulation). Time integration is performed via an implicit-explicit second-order backward difference (BDF) scheme with extrapolation for the nonlinear terms, with a time step of $dt = 0.005\delta_{\text{in}}/U_\infty$.

The LES scheme uses a relaxation-term filter to dissipate the smallest, unresolved turbulent scales[38]. This high-order filter acts directly on the resolved velocity components, $\mathbf{u}$, affecting only the small scales in the flow while leaving the larger scales unaffected[39]. The resolution of the grid in the streamwise and spanwise directions is $\delta x_1^+ \approx 27.5$ and $\delta x_3^+ \approx 16.5$, respectively, while the distance of the first (Gauss-Lobatto-Legendre) node from the wall is $\delta x_{2,w}^+ \approx 1.0$. Hence, the resolution corresponds to a well-resolved LES, similar to[40]. The superscript "+" denotes quantities scaled in terms of the viscous length $l = \nu/u_\tau$, where ν is the kinematic viscosity, $u_\tau = \sqrt{\tau_w/\rho}$ the friction velocity, τ_w the wall shear stress at the inlet, and ρ is the density of the flow.

1. Boundary Conditions

There are several ways to specify or generate the inlet conditions for a turbulent boundary layer in direct numerical simulations or large-eddy simulations. One possibility is to have a laminar inflow and then 'trip' the boundary layer[41] using a roughness strip or a random force field. Such a procedure however leads to a long transition zone and thus is not the most efficient use of the computational domain. An alternate approach involves re-scaling turbulence from downstream and/or using an auxiliary simulation to generate suitable turbulent inflow conditions[42]. A third possibility is to employ a synthetic turbulence generator (STG) to provide appropriate conditions at the inlet. A turbulent inflow profile generated using the synthetic turbulence generator (STG) described in Shur *et al.*[43] is adopted in the present work with the statistics of a ZPG TBL at the desired Reynolds number of $Re_\theta = 1551$ obtained from Jiménez *et al.*[44]. The STG of Shur *et al.*[43] can be described as follows. The velocity at the inlet is first decomposed into a mean and fluctuating component

$$\mathbf{u}(\mathbf{x},t) = \mathbf{U}_{mean}(\mathbf{x}) + \mathbf{u}'(\mathbf{x},t), \tag{3}$$

where $\mathbf{U}_{mean}(\mathbf{x})$ is the mean velocity profile and $\mathbf{u}'(\mathbf{x},t)$ is the synthetic turbulent fluctuation that is defined such that the second-moment tensor $\langle u_i' u_j' \rangle$ at the inlet is equal to the Reynolds stress tensor at $Re_\theta = 1551$. The fluctuating component is generated by superimposing $N = 285$ Fourier modes such that the power spectrum of the kinetic energy of the resulting vector follows a modified von Karman spectrum. For more details regarding the implementation of the STG, the reader is referred to Ref. 43.

To obtain the desired adverse-to-favorable pressure gradient, the top boundary condition is specified similarly to Ref. 45 as

$$u_2(x_1, L_2, x_3, t) = V_{top}(x_1), \tag{4}$$

$$\left.\frac{\partial u_1}{\partial x_2}\right|_{x_1,L_2,x_3,t} = \frac{dV_{top}(x_1)}{dx_1}, \tag{5}$$

$$\left.\frac{\partial u_3}{\partial x_2}\right|_{x_1,L_2,x_3,t} = 0, \tag{6}$$

where the top wall-normal velocity is prescribed and the streamwise and spanwise velocities adjust themselves by imposing a zero-vorticity condition, to avoid numerical oscillations. Following Ref. 46, the prescribed wall-normal velocity $V_{top}(x_1)$ follows a suction-blowing distribution described by

$$V_{top}(x_1) = -V_{max}\frac{x_1 - x_b}{\sigma_b^2}\exp\left(-\frac{1}{2}\frac{(x_1 - x_b)^2}{\sigma_b^2}\right) + V_{bleed}. \tag{7}$$

The strength of the pressure gradient is controlled by V_{max}, the streamwise extent of the separation bubble by σ_b, and the streamwise location of the peak of the adverse-to-favorable pressure gradient by x_b. In addition, a small bleed velocity V_{bleed} is imposed to ensure that the pressure gradient before and after the separation bubble remains close to zero.

Furthermore, a no-slip boundary condition is imposed at the wall ($x_2 = 0$), periodic boundary conditions at $x_3 = 0$ and $x_3 = L_3$, and a stress-free boundary condition at the outlet ($x_1 = L_1$), in order to allow the turbulent structures to leave the computational domain smoothly.

B. Actuator

Since the goal of this work is to move high-momentum LSMs toward the wall, it is essential to use an actuator that can generate on-demand regions of downwash with sizes on the order of the boundary layer thickness. Practical implementations of wall-mounted actuators that can actively generate downwash include active vortex generators[47], dielectric barrier discharge plasma actuators[48] and jet-assisted surface-mounted actuators[31].

In the numerical simulations, the actuator is modeled as a near-wall body force field (force per unit mass, i.e. acceleration, in Eq. (1)) described by

$$\mathbf{f}(\mathbf{x},t) = \mathbf{e}_\phi \tilde{g}(\mathbf{x})\tilde{f}(t). \tag{8}$$

In the above:

- $\mathbf{e}_\phi = \begin{bmatrix}\cos(\phi) & \sin(\phi) & 0\end{bmatrix}$ is the direction of the force field, which has a pitch angle toward the wall of $\phi = -\pi/3$. The angle is empirically chosen to create both near-wall acceleration and flow toward the wall.
- $\tilde{g}(\mathbf{x})$ is the spatial distribution of the force field, which follows a Gamma distribution in the streamwise direction and a Gaussian distribution in the wall-normal and spanwise directions, and is given by

$$\tilde{g}(\mathbf{x}) = \begin{cases} g(\mathbf{x}) & \text{if } g(\mathbf{x}) > 0.01, \\ 0 & \text{otherwise,} \end{cases} \tag{9}$$

where

$$g(\mathbf{x}) = \frac{x_1 - x_{1,J}}{\sigma_{1,J}} \cdot \exp\left(1 - \frac{x_1 - x_{1,J}}{\sigma_{1,J}}\right) \cdot \exp\left(-\frac{1}{2}\frac{x_2^2}{\sigma_{2,J}^2}\right) \cdot \exp\left(-\frac{1}{2}\frac{(x_3 - x_{3,J})^2}{\sigma_{3,J}^2}\right), \tag{10}$$

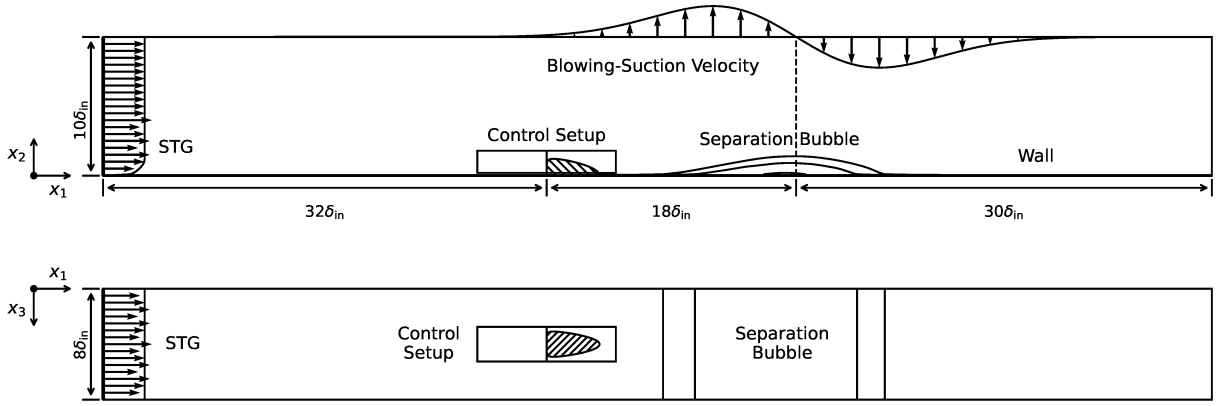

FIG. 1: Numerical Setup.

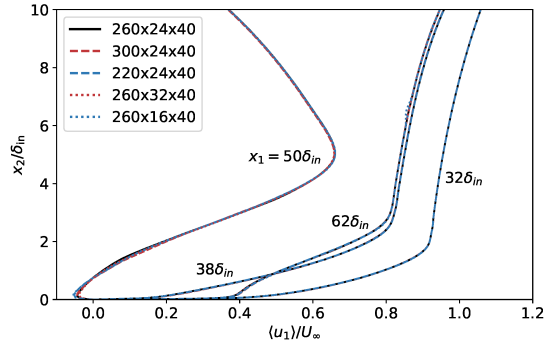

(a)

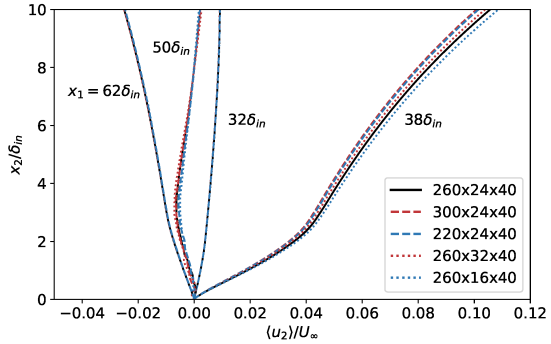

(b)

FIG. 2: Grid independence study. Velocity profiles at different x_1 locations upstream and near the separation bubble. (a) Mean streamwise velocity. (b) Mean wall-normal velocity. The grid sizes indicate the number of elements in each direction (e.g., $260\times24\times40$ corresponds to $N_1 = 260$, $N_2 = 24$, and $N_3 = 40$).

with $\mathbf{x}_J = \begin{bmatrix} x_{1,J} & 0 & x_{3,J} \end{bmatrix}$ the location of the jet and $\sigma_{1,j}$, $\sigma_{2,j}$, $\sigma_{3,j}$ the positive scalars that control the streamwise, wall-normal and spanwise extent of the jet.

- $\tilde{f}(t)$ is the scalar-valued function of time that controls the magnitude of the overall force field such that the power input is constant and equal to $p(t)$.

The control input to the actuator is a binary time-varying signal $p(t) \in \{0, G\}$ that controls whether or not a constant amount of power will be added to the flow at each time step. In particular, since the power $p(t)$ is defined as

$$p(t) = \int_{\mathcal{V}} \rho \mathbf{f}(\mathbf{x},t) \cdot \mathbf{u}(\mathbf{x},t) \mathrm{d}\mathcal{V} \tag{11}$$

$$= \tilde{f}(t)\rho \int_{\mathcal{V}} \tilde{g}(\mathbf{x}) \mathbf{e}_\phi \cdot \mathbf{u}(\mathbf{x},t) \mathrm{d}\mathcal{V} \tag{12}$$

$$= \tilde{f}(t) I(t), \tag{13}$$

where $I(t)$ is the volumetric integral of the power per unit force $\tilde{f}(t)$, then

$$\tilde{f}(t) = p(t)/I(t). \tag{14}$$

The model predictive control scheme presented in this work aims to determine the optimal control policy that the input signal $p(t)$ has to follow, such that only high-momentum LSMs will be moved toward the wall. When the jet is on ($p(t) = G$), the $\phi = -\pi/3$ pitch angle of the force field leads to the acceleration of the flow both downstream and toward the wall. A localized region of downwash ($u_2' < 0$, Fig. 3) is created near the core of the force field that then travels downstream. At the same time, two smaller lobes of upwash ($u_2' > 0$) are created on both sides of the downwash. Depending on how long the jet force field remains on, longer or shorter regions of downwash can be created.

TABLE II: Jet force field parameters.

	G	$x_{1,J}$	$x_{3,J}$	$\sigma_{1,J}$	$\sigma_{2,J}$	$\sigma_{3,J}$	ϕ
Baseline	0.02	32	4	0.5	0.4	0.3	$-\pi/3$

The baseline actuator force field parameters are given in Table II. The height of the force field, controlled by $\sigma_{2,J}$ is chosen such that the region of strong downwash ($u_2' < -0.025$) extends to the outer region of the boundary layer, where the LSMs of interest can be found. The streamwise extent of the

force field, which is approximately $4\delta_{in}$, is chosen to correspond to a typical length of an LSM. However, the streamwise length of the created downwash region can also be controlled by the time the jet remains on, making the exact value of $\sigma_{1,J}$ less critical. In the spanwise direction, $\sigma_{3,J}$ is chosen to create downwash in a span of approximately δ_{in}. The jet parameter with the most notable contribution to the performance of the scheme is the power input, G, to the jet when it is on ($p(t) = G$), which directly determines the strength of the jet force field. The effect of the parameter G on the flow reattachment is further studied in Section IV.

III. CONTROL SCHEME

A. Overview

The primary objective for separation delay is to increase the near-wall momentum at the area where separation occurs. One could formulate an optimal control problem where the objective is to maximize the streamwise momentum at a location downstream of the actuator. However, such a formulation would not ensure that LSMs are considered when determining the optimal control input, as the interaction of LSMs with the actuator-induced flow field and the resulting streamwise momentum increase can be highly nonlinear and challenging to model.

Since the present study aims to extract additional performance gains by exploiting the energy contained in LSMs, a *surrogate* optimal control problem is formulated. To render the above control problem tractable using linear reduced-order models, the objective of the surrogate optimal control problem is defined as the maximization of the jet-induced downwash experienced by the LSMs of interest (i.e., high-momentum LSMs), along with the minimization of power consumption (i.e., the amount of time the actuator is on). Specifically, the controller is designed as a model predictive control scheme with three main components: 1) detection of the LSMs of interest, 2) prediction of LSM trajectories using Taylor's hypothesis, and 3) maximization of the downwash encountered by the LSMs of interest along their predicted trajectory.

LSMs of interest are detected upstream of the actuator within a *measurement grid*. The jet-induced wall-normal velocity field near the actuator is modeled in a *control grid* using a linear reduced-order model. With LSM measurements from the measurement grid, LSMs in the control grid are predicted using Taylor's hypothesis. Then, the control input that solves the surrogate optimal control problem is determined through a binary optimization problem.

B. Measurement Grid

The first step of the control scheme is to detect the regions of large-scale streamwise velocity fluctuations u_1' *upstream* of the actuator. In the present work, the raw velocity fluctuations u_1' are directly measured on a sub-sampled orthogonal grid located directly upstream of the jet force field. This choice is made to simplify the detection scheme and avoid potential errors that could arise from estimating the location of LSMs indirectly from wall shear stress or pressure measurements (e.g., Refs. 27 and 28). This measurement grid has $51\times17\times26$ grid points in the streamwise, wall-normal, and spanwise directions, respectively, and spans $5\delta_{in}\times1.6\delta_{in}\times2.5\delta_{in}$ (Fig. 4). It is centered at $x_3 = x_{3,J}$ and spans from $x_1 = 27\delta_{in}$ to $x_1 = 32\delta_{in}$. Furthermore, the first grid point from the wall is located at $x_2 = 0.2\delta_{in}$, such that only the logarithmic and outer layers of the boundary layer contribute to the fluctuation measurements. This is an important choice for prioritizing moving high-momentum regions from the outer parts of the boundary layer toward the wall rather than expending control efforts on high-momentum regions already close to the wall.

1. Box Filtering

Once the velocity fluctuations u_1' at the measurement grid have been obtained at a given time step, a box filter is applied to the 3D measurement, such that the smaller scales are filtered out, and only the largest scales remain. Here, the filter of choice is the $7\times7\times7$ uniform convolution kernel that is applied to the measurement $u_1'(t)[i,j,k]$ at each grid point $[i,j,k]$ as

$$\tilde{u}_1'(t)[i,j,k] = \frac{1}{7^3}\sum_{m_1=-3}^{3}\sum_{m_2=-3}^{3}\sum_{m_3=-3}^{3} u_1'(t)[i+m_1, j+m_2, k+m_3] \tag{15}$$

for $i = 0,\ldots,100$, $j = 0,\ldots,16$, and $k = 0,\ldots,25$. An example of a 3D measurement of u_1' sub-sampled from the LES grid to the measurement grid before and after applying the box filter is given in Fig. 5. It can be seen that the filtering operation leads to a u_1' velocity field where the large-scale high and low momentum regions are clearly visible, while the smaller scales, which are not of interest in the proposed control scheme, are eliminated.

An alternative filtering method for isolating the largest scales in a flowfield snapshot is Gaussian filtering, which has been used in works such as Refs. 33 and 49. However, a simple box filter like the one used in this work is deemed appropriate here due to its simplicity (only one parameter to tune, i.e. the box size) and effectiveness in filtering out small-scale structures.

C. Control Grid

The second part of the control setup is the control grid. The control grid has the same size and number of grid points as the measurement grid but is translated by $5\delta_{in}$ downstream relative to it. As a result, the control grid begins at $x_1 = 32\delta_{in}$, i.e. where the measurement grid ends and the jet force field begins, and both grids share the nodes at $x_1 = 32\delta_{in}$ (Fig. 4).

The control grid is strategically placed to cover the immediate neighborhood of the actuator, where the downwash is created. The purpose of this grid is twofold. First, the LSMs

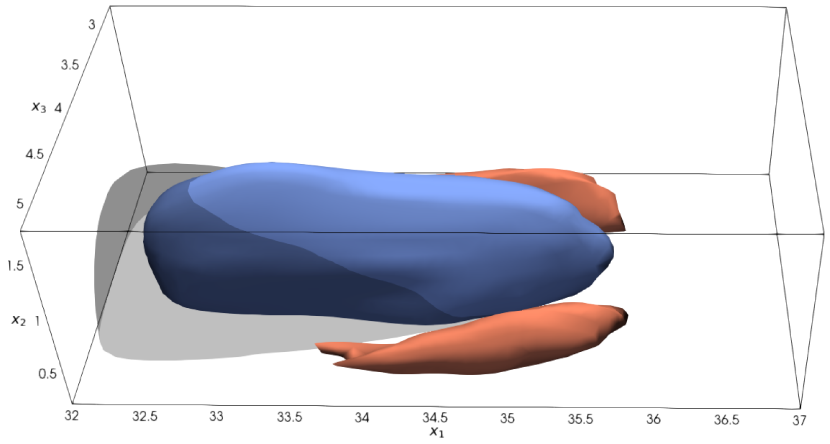

(a) 3D isosurfaces of downwash $u_2' = -0.1$ (blue), upwash $u_2' = 0.1$ (red), and jet force field $g(\mathbf{x}) = 0.01$ (transparent gray).

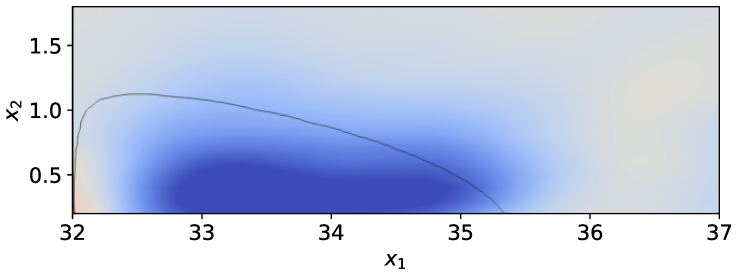

(b) Contour of u_2' on a spanwise-normal plane across the center of the jet.

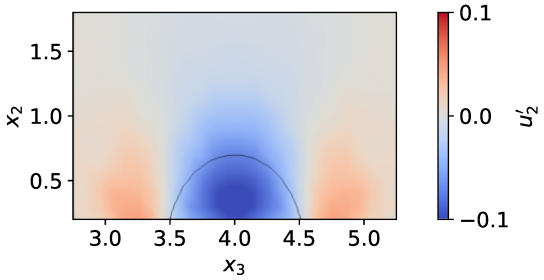

(c) Contour of u_2' on a streamwise-normal plane at $x_1 = 34\delta_{\text{in}}$.

FIG. 3: Wall-normal velocity fluctuations induced by the jet force field. The velocity fluctuations are obtained by first ensemble-averaging the turbulent flow snapshots and then smoothing using the first 8 POD modes of 500 ensemble-averaged snapshots, in order to discern the effects of the jet from the background turbulence.

of interest that are detected in the measurement grid are assumed to convect downstream with the mean velocity field. Thus, the filtered u_1' fluctuations in the control grid are predicted via Taylor's hypothesis (see Subsection III D). Second, the dynamics of the wall-normal velocity fluctuations u_2' at the control grid points induced by the jet for a given control input are modeled via a total-least-squares dynamic mode decomposition with control (tlsDMDc) reduced-order model (see Subsection III E).

These two components – knowing where the LSMs are located within the control grid and having a model of the downwash that can be created within the same grid – are essential for designing a model-based controller that is optimal in the sense that it maximizes the downwash in the location of high-momentum LSMs in the control grid while avoiding low-momentum ones and minimizing actuation effort.

D. Taylor's Hypothesis for Predicting LSM Trajectories

Large-scale motions need to be detected upstream of the actuator to minimize the influence of the actuator-induced flow-field on the measurement of streamwise velocity fluctuations and to give enough time to the actuator to respond. As actuation occurs in the control grid, which is downstream of the measurement grid, there is a delay before the detected LSMs reach the actuator. Therefore, it is necessary to predict the location of the LSMs over the next few time steps before deciding whether to activate the actuator or not. This requires predicting the streamwise velocity fluctuations in the control grid based on measurements obtained in the measurement grid. To do that, Taylor's hypothesis is employed.

Taylor's frozen turbulence hypothesis[1,32] states that the small-scale turbulence in a fluid flow remains frozen in shape and structure as it convects downstream with the large-scale (i.e., mean) velocity. In other words, the hypothesis suggests that turbulent structures of different length scales can be considered as separate and distinct entities, with each structure evolving independently of one another.

In the context of a turbulent boundary layer, the hypothesis can be stated as

$$\mathbf{u}(x_1, x_2, x_3, t) = \mathbf{u}(x_1 - U_c\tau, x_2, x_3, t - \tau) \tag{16}$$

for relatively small values of time delay τ. In the above, U_c is the convection velocity, which is typically chosen to be the

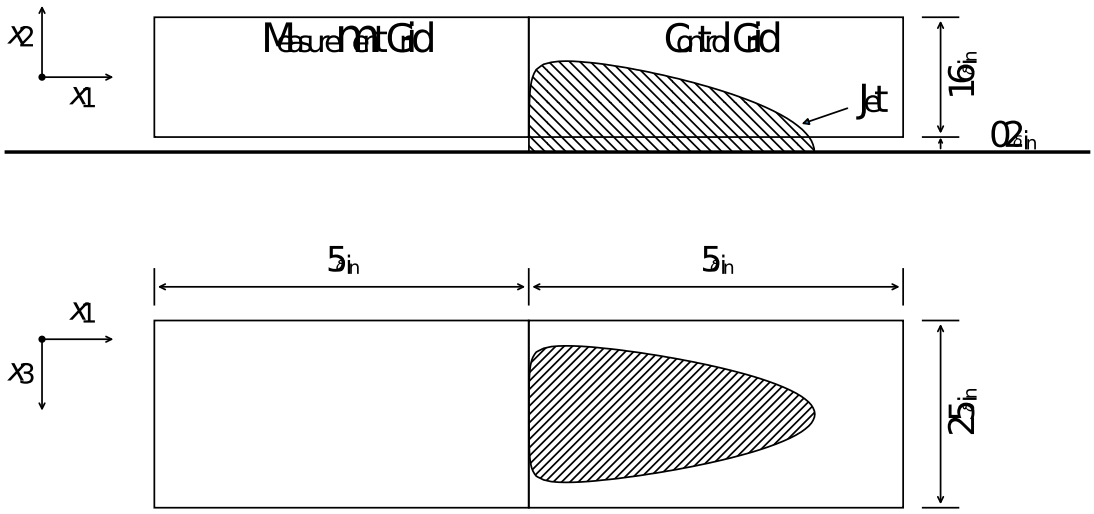

FIG. 4: Control setup. The location and size of the measurement and control grids, along with an isosurface of the jet force field distribution ($g(\mathbf{x}) = 0.01$), are illustrated.

mean streamwise velocity at the given streamwise and wall-normal location, i.e. $U_c = U_c(x_1, x_2)$. This approximation has been observed to be accurate for boundary layers, as long as the velocity fluctuations $\mathbf{u}'$ are relatively small[33]. Although the convection velocity is typically assumed to be the mean velocity profile, it has been observed through space-time correlations of experimental flowfield measurements that the convection velocity tends to be higher than the local mean near the wall (up to the logarithmic layer) and smaller than the mean in the outer logarithmic and wake regions[50]. Similar observations have also been made for channel flows[34]. However, it is also expected that the actuator will induce an acceleration in the streamwise component that will counteract the slower convection of the outer LSMs. Therefore, the convection velocity in this study is taken to be equal to the mean, before actuation.

In practice, the proposed control scheme needs to take into account the velocity fluctuations at the control grid over the next few time steps, starting from the current time step, t. Let $u'_{1,M}$ be the streamwise velocity fluctuations measured at the measurement grid and $u'_{1,C}$ the predicted streamwise velocity fluctuations at the control grid. The predicted value of $u'_{1,C}$ at some future time step $t+k$ according to Taylor's hypothesis and using measurements up to time step t is

$$u'_{1,C}(x_1, x_2, x_3, t+k) = u'_{1,M}(x_1 - U_c \tau T_{rom}, x_2, x_3, t+k-\tau), \tag{17}$$

where the time delay τ is chosen such that

$$27\delta_{\text{in}} \leq x_1 - U_c \tau T_{rom} \leq 32\delta_{\text{in}}, \tag{18}$$

$$t+k-\tau \leq t, \tag{19}$$

i.e. the measurement is coming from within the measurement grid and has already been obtained. Furthermore, it is desired that the most recent measurement is used, i.e. $t+k-\tau$ is maximized while still corresponding to an integer time step at which a measurement was obtained. Note that the above time steps correspond to reduced-order model timesteps.

An important aspect that needs to be considered is the influence of the filtering of streamwise velocity fluctuations on the validity of Taylor's hypothesis. Assuming that the actuator is off, the correlation of the predicted streamwise velocity fluctuations with the actual measurements obtained in the control grid can be computed as

$$R_{u'_1 u'_{1,C}}(x_1, x_2, k) = \frac{\overline{u'_1 u'_{1,C}}}{\sqrt{\overline{\left(u'_1\right)^2}}\sqrt{\overline{\left(u'_{1,C}\right)^2}}}, \tag{20}$$

where u'_1 is a sample of the exact streamwise velocity fluctuations measured at the control grid at a timestep $t+k$ and $u'_{1,C}$ a sample of the velocity fluctuations predicted via Taylor's hypothesis using measurements *up to timestep* t. The operator $\overline{(\cdot)}$ denotes the time and spanwise average of the underlying quantity. A similar correlation metric can be derived for the filtered velocity components $\tilde{u}'_1$ and $\tilde{u}'_{1,C}$.

Figure 6 presents the correlation between the streamwise velocity fluctuations measured at the control grid with those predicted by applying Taylor's hypothesis. This is done for both the raw and filtered fluctuations from the measurement grid, taking into account various distances from the wall (x_2) and prediction horizons. In every case, the correlation between the box-filtered u'_1 at the control grid and the predictions using the filtered u'_1 from the measurement grid is consistently higher than the predictions utilizing the raw u'_1. Note that the correlation at $x_1 = 32$ tends to be lower than one the further ahead in time (i.e., larger k) the prediction is made.

The correlations are calculated by averaging spanwise and across a sample of 2000 different measurements for various

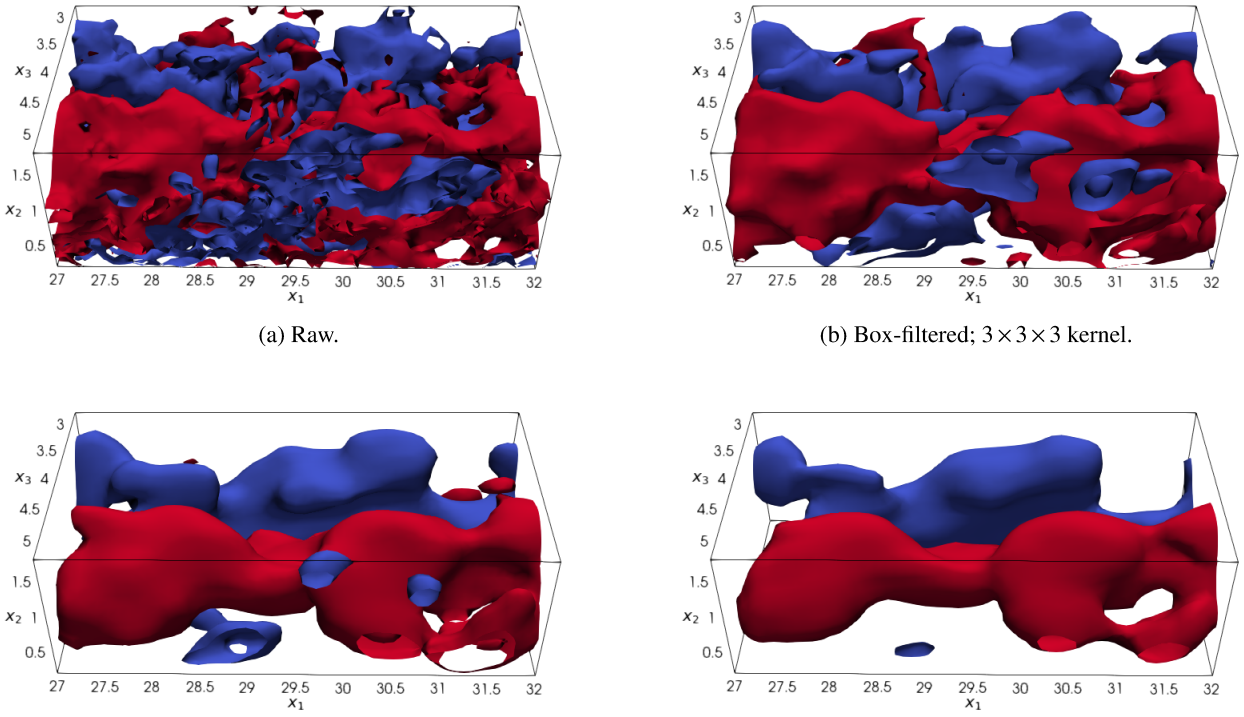

(a) Raw.

(b) Box-filtered; $3\times3\times3$ kernel.

(c) Box-filtered; $5\times5\times5$ kernel.

(d) Box-filtered; $7\times7\times7$ kernel.

FIG. 5: LSM filtering. Isosurfaces correspond to $\tilde{u}'_1 = 0.025$ (red) and $\tilde{u}'_1 = -0.025$ (blue).

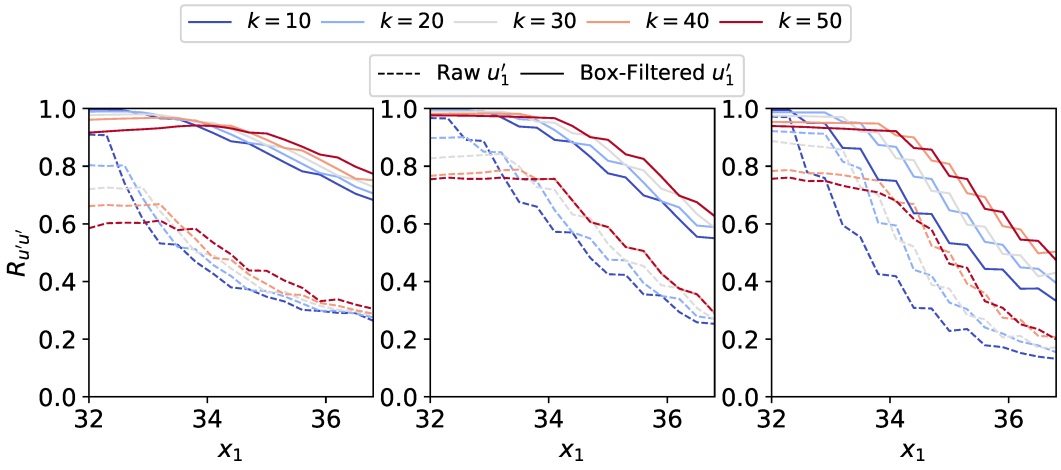

(a) $x_2 = 0.2\delta_{\text{in}}$

(b) $x_2 = 1.0\delta_{\text{in}}$

(c) $x_2 = 1.8\delta_{\text{in}}$

FIG. 6: Correlation $R_{u'_1 u'_{1,C}}$ of the predicted velocity fluctuations, $u'_{1,C}$, with the actual ones, u'_1, at different streamwise and wall-normal locations, x_1 and x_2, within the control grid, and for different time horizons k. Similar correlations for the filtered quantities $\tilde{u}'_{1,C}$ and $\tilde{u}'_1$ are also given. Each time step in k corresponds to a nondimensional time of $T_{rom} = 0.05\delta_{\text{in}}$.

prediction horizons (k timesteps in the future) relative to the last obtained measurement at timestep t. This analysis demonstrates that predicting filtered velocity fluctuations results in a stronger correlation with the actual (filtered) velocity fluctuations, leading to more accurate predictions. This finding supports the observations made by Ref. 33.

E. Actuator Reduced-Order Model

After predicting the streamwise velocity fluctuations within the control grid, the next step is to determine whether turning the actuator on ($p(t) = G$) will create enough downwash at high-momentum regions while avoiding low-momentum ones and, at the same time, minimizing actuation effort. To address this optimal control problem, a reduced-order model is employed for the dynamics of the wall-normal velocity fluctuations induced by the jet force field.

The u_2' dynamics within the control grid are modeled using total least squares dynamic mode decomposition with control (tlsDMDc). Dynamic Mode Decomposition (DMD)[51,52] is a widely-used algorithm for analyzing and modeling the dynamics of fluid flows. The algorithm decomposes a complex, high-dimensional system into a set of simple, linear, and dynamically evolving modes that describe the underlying structure and behavior of the system. This can provide insight into the underlying physics of the system and facilitate the development of predictive models that are useful for control design[53], among other tasks. The linear nature of DMD models makes them well-suited for linear optimal control techniques, which can be implemented efficiently due to the low order of the resulting system.

Since the jet force field is located within the turbulent boundary layer, ensemble averaging of the training data is performed to accurately separate the jet-induced wall-normal velocity fluctuations from the background turbulence. The control input signal used to generate the jet response is repeated multiple times and the resulting average of the wall-normal velocity fluctuations is obtained. Averaging is also carried out symmetrically across the spanwise-normal plane at $x_3 = 4\delta_{\text{in}}$ due to the symmetry of the jet force field.

However, performing LES multiple times to gather ensemble responses is cost-prohibitive. As a result, only a limited number of ensembles is collected, leading to a cleaner but still noisy dataset for the jet-induced u_2'. Throughout this study, a total of 10 ensembles are used to compute a reduced-order model for each of the presented control configurations. If the remaining small-scale turbulence is treated as noise, then a dynamic mode decomposition model that can handle noisy datasets is needed.

In order to account for the presence of measurement and process noise in the snapshot data, total least squares DMD (tlsDMD) was proposed in Ref. 35, while a similar method, named total DMD (TDMD), was proposed in Ref. 54. The robustness to measurement and process noise of these noise-aware variants of DMD makes them an attractive choice for modeling a turbulent flow. However, neither of the above methods can handle systems with control inputs. In this work, tlsDMD is extended to systems with control inputs, following a similar approach to Ref. 53. A reduced-order state-space model of the actuator dynamics is obtained using the "noisy" (turbulent) snapshots of wall-normal velocity fluctuations within the control grid. The details of extending tlsDMD to systems with control inputs are provided in Appendix A.

The training data for the present study consist of the wall-normal velocity fluctuations at the control grid collected over 10 distinct LES, where the training input signal is repeated, albeit with different background turbulence each time. The snapshots are sampled every $T_{rom} = 10$ LES time steps, or $\Delta t = 0.05\delta_{\text{in}}/U_\infty$, and the background turbulence is smoothed by ensemble-averaging the 10 different sets of measurements, as well as averaging around the symmetry plane $x_3 = 4\delta_{\text{in}}$.

It is important to note that the high computational cost of LES, combined with the necessity to ensemble average snapshots to discern the actuator's impact on the turbulent flow, can make using a lengthy training input signal prohibitive. As a result, the training input must be strategically selected to extract the dominant modes the actuator is anticipated to display during operation. Specifically, since the jet will target LSMs with spatial coherence on the order of the boundary layer thickness δ_{in}, the actuator is expected to remain active for periods on the order of $\delta_{\text{in}}/U_\infty$. For that reason, the training input is chosen to consist of three pulses with durations of $2\delta_{\text{in}}/U_\infty$, $4\delta_{\text{in}}/U_\infty$, and $6\delta_{\text{in}}/U_\infty$, ensuring sufficient time between each pulse for the jet-induced flowfield to subside.

The control input used to generate the training data is shown in Fig. 7a. An additional validation dataset is obtained using a control input consisting of a different set of three random-width pulses, also shown in Fig. 7a. Both datasets contain 560 snapshots. The ability of the computed tlsDMDc models to predict the wall-normal velocity fluctuations at the control grid is evaluated on both the training and validation data. Specifically, using the control input of each dataset (training and validation), a 560-time-step prediction is made using the linear reduced-order model and a zero initial condition, and the average error between the predicted flowfield, $\mathbf{y}_{pred}(k)$, and the exact flowfield, $\mathbf{y}_{exact}$, obtained by ensemble-averaging, is computed and normalized by the average snapshot in each dataset. The errors are given in Fig. 7b. Even though the relative errors appear to be large due to the unmodeled small-scale structures that are present in the snapshots, qualitatively, the predictions appear to agree with the large-scale influence of the jet. This is demonstrated in Fig. 8, where the predicted velocity field u_2' (which does not include small-scale turbulence) compares favorably with an ensemble-averaged snapshot, where small scales are still present, despite the ensemble-averaging. Due to the need for computational efficiency when executing the proposed control algorithm, a model with $n_z = 7$ modes is selected as a compromise between prediction accuracy and model order.

F. Optimal Output Tracking Controller

With both the streamwise velocity fluctuations and the dynamics of the wall-normal velocity induced by the jet on the control grid nodes known, finding the control input that maximizes the downwash encountered by high-momentum LSMs can be expressed as follows.

Problem Formulation: Among the admissible control policies $\pi_t = \left\{p(t),\ \cdots,\ p(t+N_{mpc}-1)\right\}$, such that $p(k) \in \{0, G\}$ for all $k = t, \ldots, t+N_{mpc}-1$, find an optimal control policy $\pi_t^* = \left\{p^*(t),\ \cdots,\ p^*(t+N_{mpc}-1)\right\}$ that solves the optimization

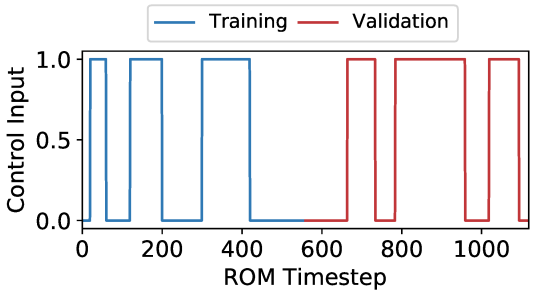

(a) Control inputs.

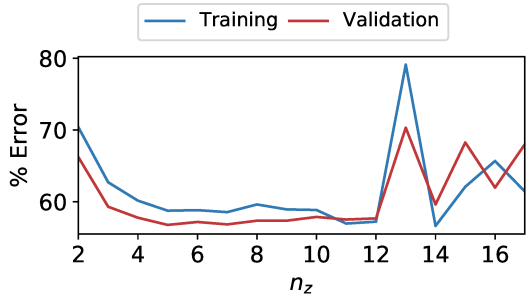

(b) Prediction errors.

FIG. 7: Training and validation of the tlsDMDc reduced-order model.

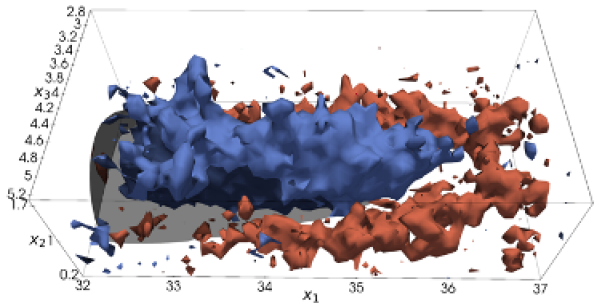

(a) Ensemble-averaged snapshot.

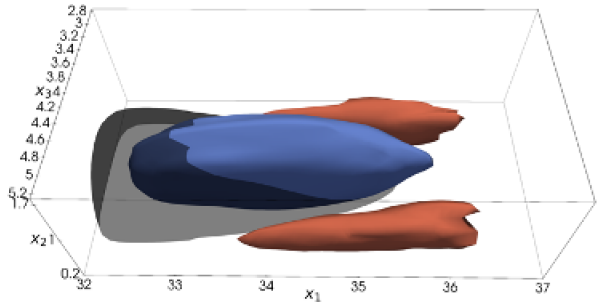

(b) Predicted snapshot.

FIG. 8: A sample of an ensemble-averaged snapshot versus a snapshot predicted with the ROM (with $n_z = 7$ modes) on the validation dataset. 3D isosurfaces of downwash $u_2' = -0.1$ (blue), upwash $u_2' = 0.1$ (red), and jet force field $g(\mathbf{x}) = 0.01$ (transparent gray).

problem

$$\begin{aligned} \pi_t^* = \arg\min_{\pi_t} \quad & \sum_{k=t}^{t+N_{mpc}-1} rp^2(k) + \|\mathbf{y}(k+1) - \mathbf{y}_{des}(k+1)\|_Q^2 \\ \text{subject to} \quad & \mathbf{z}(k+1) = A\mathbf{z}(k) + Bp(k),\ k = t,\ldots,t+N_{mpc}-1 \\ & \mathbf{y}(k) = C\mathbf{z}(k),\ k = t,\ldots,t+N_{mpc} \\ & p(k) \in \{0,\ G\},\ k = t,\ldots,t+N_{mpc}-1 \\ & \mathbf{z}(t) = \tilde{\mathbf{z}}(t). \end{aligned} \tag{21}$$

If $\mathbf{v}(t+1),\ \cdots,\ \mathbf{v}(t+N_{mpc})$ is the (vectorized) filtered streamwise velocity fluctuations $\tilde{u}'_{1,C}$ predicted with Taylor's hypothesis at the control grid over the next N_{mpc} time steps and using measurements up to the current time step t, then the desired output $\mathbf{y}_{des}$ of the reduced-order model can be defined as

$$\mathbf{y}_{des}(k) = -\lambda \mathbf{v}(k), \quad \forall k = 1,\ldots,N_{mpc} \tag{22}$$

with $\lambda > 0$ a scaling factor that maps regions of high momentum ($u'_1 > 0$) within the control grid to regions of desired downwash ($u'_2 < 0$), while low-momentum ones are mapped to regions of upwash. Note that $\tilde{z}(k)$ is a previous estimate of the ROM state.

The above can be formulated as an integer quadratic program (IQP) with

$$\boldsymbol{\pi} = [p(t),\ \cdots,\ p(t+N-1)]^{\mathrm{T}}$$

the decision variable. However, the complexity of an IQP is NP-hard and can be prohibitively expensive to solve. Here, the above problem is solved by relaxing the integer input to a continuous one ($p(k) \in \mathbb{R}$), with the additional constraint of

$$Gp(k) = p^2(k)$$

that is satisfied only when $p(k) = 0$ or $p(k) = G$. The problem can then be cast to a semi-definite program with linear constraints and solved efficiently[55]. In particular, the optimal output tracking control problem (OTC) in (21) (after its semi-definite relaxation) can be considered as a stand-alone module of the form

$$\pi_t^* = \mathcal{OTC}\big(A, B, C, r, Q, \tilde{\mathbf{z}}(t), \mathbf{y}_{des}(t+1), \ldots, \mathbf{y}_{des}(t+N)\big) \tag{23}$$

The details of implementing the above semi-definite program are provided in Appendix B.

G. Model Predictive Control

The individual components of the control scheme presented so far can now be composed to design a systematic controller under the model predictive control (MPC) framework. The key idea behind MPC is to predict the system's future behavior using an available model and then optimize the control signal over a finite time horizon to achieve the desired performance.

The optimized control input is then applied to the system, and the process is repeated at frequent time steps.

In the proposed scheme, the two quantities of interest within the control grid are: the streamwise velocity fluctuations, which are predicted using Taylor's hypothesis, and the jet-induced wall-normal velocity, which is estimated using the tlsDMDc reduced-order model. To solve the optimal output tracking control problem, these predictions are utilized to identify the optimal input that maximizes the overlap between downwash and LSM within the control grid. The optimization process yields the optimal input, which is then implemented in the LES until new measurements are obtained, at which point the procedure is repeated. The MPC algorithm for targeting LSMs is given in Algorithm 1.

The optimal control problem is solved over a horizon of $N_{mpc} = 50$ ROM time steps, which corresponds to a time horizon of $\Delta t = 2.5\delta_{\text{in}}/U_\infty$. However, new measurements are taken into account every $N_{meas} = 5$ ROM time steps, or $\Delta t = 0.25\delta_{\text{in}}/U_\infty$. As a result, the optimal input from each optimization step is applied only for the first $\Delta t = 0.25\delta_{\text{in}}/U_\infty$ before the optimal control problem is resolved using the updated measurements. Figure 9 provides a visual representation of the distinct timelines involved in the MPC algorithm.

The rationale behind selecting the aforementioned time steps is twofold. First, the MPC horizon is chosen to be sufficiently long to accommodate any actuation delays, as the jet force field does not generate downwash instantaneously. Second, the frequency at which new LSM measurements are considered, and consequently, the optimal input is updated, is determined to be frequent enough to account for medium-scale motions (e.g., with streamwise lengths of less than δ_{in}) but not so frequent that the computational cost becomes prohibitively high. Comprehensive investigations on the impact of these two time scales have led to the adoption of the specified time horizons.

Algorithm 1 Model Predictive Control of LSMs

procedure MpcOfLsms(N_{mpc}, N_{meas}, T_{rom}, A, B, C, r, Q)
  $\tilde{\mathbf{z}}(0) \leftarrow 0$
  for $i = 0, 1, \ldots$ **do**
    $t \leftarrow \lfloor i/T_{rom} \rfloor$ ▷ Integer division of i by T_{rom}
    if $i \mod (N_{meas} * T_{rom}) == 0$ **then**
      ▷ Detect LSMs
      Measure u_1' on Measurement Grid
      $\tilde{u}_1' \leftarrow$ filtered u_1'

      ▷ Predict LSMs on Control Grid
      for $j = 1, \ldots, N_{mpc}$ **do**
        $\tilde{u}_{1,T}'(t+j) \leftarrow$ Taylor's hypothesis on $\tilde{u}_1'$ for j steps
      end for

      ▷ Map predicted fluctuations to desired ROM output
      for $j = 1, \ldots, N_{mpc}$ **do**
        $\mathbf{y}_{des}(t+j) \leftarrow -\lambda \tilde{u}_{1,T}'(t+j)$
      end for

      ▷ Solve optimal output tracking control problem
      $p^*(t), \ldots, p^*(t+N_{mpc}-1) \leftarrow \mathcal{OTC}\big(A, B, C, r, Q, \tilde{\mathbf{z}}(t), \mathbf{y}_{des}\big)$

      ▷ Propagate ROM by N_{meas} time steps
      for $j = 0, \ldots, N_{meas} - 1$ **do**
        $\tilde{\mathbf{z}}(t+j+1) \leftarrow A\tilde{\mathbf{z}}(t+j) + Bp^*(t+j)$
      end for
    end if
    Apply control input $p^*(t)$ in Large Eddy Simulation
  end for
end procedure

IV. RESULTS

The control scheme presented in Section III is implemented in the LES of Section II. The focus is on targeting *high-momentum LSMs* to increase the near-wall momentum and reduce the size of the separation bubble. To evaluate the performance of the proposed scheme, four control schemes are considered, as shown in Table III.

TABLE III: Actuation schemes being compared in the present study.

Scheme	Targets	Power Input	Duty Cycle
Targeting fast LSMs	$\tilde{u}_1' > 0$	G	0.5 ± 0.01
Targeting slow LSMs	$\tilde{u}_1' < 0$	G	0.5 ± 0.01
Random actuation	$\tilde{u}_1' > 0$ and $\tilde{u}_1' < 0$	G	0.5 ± 0.02
Constant actuation	$\tilde{u}_1' > 0$ and $\tilde{u}_1' < 0$	$0.5 \times G$	1.0

The control inputs for the fast and slow LSM targeting cases are denoted by p_F^* and p_S^*, respectively, where the superscript $*$ indicates optimality with respect to Problem (21). For the random and continuous actuation cases, the control inputs are denoted as p_R and p_C, respectively.

In all cases, the synthetic turbulent inflow condition is the same, meaning that all cases are expected to encounter the "same" turbulence – at least up to the proximity of the control jet, near which the flow structures are affected by the jet. Targeting slow LSMs is considered the "opposite" of targeting fast LSMs. The control inputs for the two cases tend to be the opposite of each another, as one would expect: when the jet is on in one case, the jet in the other case is off. Switching to slow targets from fast ones can be done by setting $\lambda < 0$ in (22). In both of these cases, if the control scheme is applied for long enough (e.g., $> 500\delta_{\text{in}}/U_\infty$), the average optimal control input converges to $0.5G$. This is expected since about half of the domain should contain fast LSMs and the other half slow LSMs.

For the random actuation case, a random binary signal with an average value of $0.5G$ is used. To generate an input that is qualitatively similar to the fast and slow targeting cases but not correlated with the presence of LSMs in the control grid, a random signal is generated using the power spectral density (PSD) of p_F^* and p_S^*. Since both control inputs have (approximately) the same frequency content, Welch's method[56] is used to compute the PSD of p_F^* and p_S^*. Then, a random continuous signal $\tilde{p}_R$ is generated using the computed PSD. Finally, $\tilde{p}_R$ is converted to a binary signal by setting $p_R = G$ if $\tilde{p}_R > 0$ and $p_R = 0$ otherwise. This leads to a control input that is qualita-

FIG. 9: The MPC horizon compared to the frequency with which the MPC problem is resolved.

tively similar to the optimal inputs p_F^* and p_S^* but with a low correlation to either of the two signals.

The final case considered is a continuously actuated jet, i.e., a jet that is constantly on, albeit at 50% the strength of the other three cases. In other words, $p_C = 0.5G$ for all time steps t. The reduction of the continuous jet strength by 50% is motivated by the fact that in all other cases, the duty cycle is 50%, whereas the continuous jet is always on. The control inputs for each case over a total test time of $800\delta_{\text{in}}/U_\infty$ (i.e. 10 flow-through times) are given in Fig. 10

In addition to the control input, another important parameter that is explored is the power input G, which controls the overall strength of the jet. Three power input values are considered, as shown in Table IV.

TABLE IV: Power inputs considered in the present study.

Case	Power Input G
Weak Jet	0.01
Baseline Jet	0.02
Strong Jet	0.03

For each power input, all four actuation schemes are implemented, resulting in a total of 12 cases in addition to the case with no actuation. Each case is run for a total of $800\delta_{\text{in}}/U_\infty$, corresponding to 10 flow-through times, with each simulation consuming approximately 100000 CPU hours.

A. Validation of the Control Scheme

In order to ensure that the control scheme is indeed targeting high-momentum LSMs, a separate simulation is run, where the streamwise velocity fluctuations, u_1', are conditionally averaged only when $p_F^* > 0$, i.e., when fast LSMs are targeted. However, no actuation occurs in order to avoid polluting the conditionally-averaged flowfield with the effects of the jet. This conditional average, $\langle u_1' \rangle_{p>0}$, is illustrated in Fig. 11. It can be seen that upstream and close to the center of the jet, the average velocity fluctuations are positive, i.e., they correspond to fast LSMs. Conversely, slow LSMs are seen on the sides of the jet. The presence of fast LSMs upstream of the location of the jet force field also indicates that the control scheme is taking into account the delay between the jet turning on and downwash being created. This confirms that, indeed, the control scheme targets high-momentum LSMs, as expected.

B. Mean Effect on Separation

While the flow is homogeneous when no actuation is present, the introduction of the jet in the middle (spanwise) of the domain breaks the homogeneity in the x_3 direction due to the inhomogeneity of the body force field but introduces symmetry around the $x_3 = 4\delta_{in}$ plane. Therefore, in order to capture the mean effect that the actuation scheme has on the flow, the time and symmetry averaged flow is considered, leading to a total time horizon for averaging of $1600\delta/U_\infty$.

First, the reduction of the time-average separation bubble is considered. For each case, both the volume of the reverse flow,

$$V = \int_{\mathcal{V}} I(\langle u_1 \rangle < 0) \mathrm{d}\mathcal{V} \tag{24}$$

and the area of negative streamwise wall shear stress on the wall

$$A = \int_{\mathcal{A}_w} \left(\left. \frac{\partial \langle u_1 \rangle}{\partial x_2} \right|_{x_2=0} < 0 \right) \mathrm{d}\mathcal{A}_w \tag{25}$$

are computed, in ${\delta_{\text{in}}}^2$ and ${\delta_{\text{in}}}^3$ units, respectively. In the above, $\mathcal{V}$ is the computational (3D) volume, $\mathcal{A}_w$ is the surface of the 2D wall and $I(a)$ is the indicator function such that,

$$I(a) = \begin{cases} 1, & \text{if } a \text{ is true} \\ 0, & \text{otherwise.} \end{cases} \tag{26}$$

The results of the above values for each case are given in Fig. 12. The mean and standard deviation values presented are the statistics of a windowed-average approach, where mean values are obtained for two cases: a window from $t = 0$ to $t = 560\delta_{\text{in}}/U_\infty$ and another from $t = 240\delta_{\text{in}}/U_\infty$ to $t = 800\delta_{\text{in}}/U_\infty$. The window length is long enough (7 flow-through times) to ensure that the average duty cycle in all cases is 50%. However, due to the large computational cost of the simulations, obtaining statistics for a larger number of windows is impractical.

For the baseline case, targeting fast LSMs leads to the biggest decrease in both the separation volume and area. In particular, there is an approximately 42% decrease in the average separation volume and 38% in the separation area, compared to 28% and 25.0% for the slow targets, respectively. Decreasing the strength of the jet G leads to targeting fast LSMs performing better than the other actuation schemes in decreasing the volume of separation, but the decrease in the separated

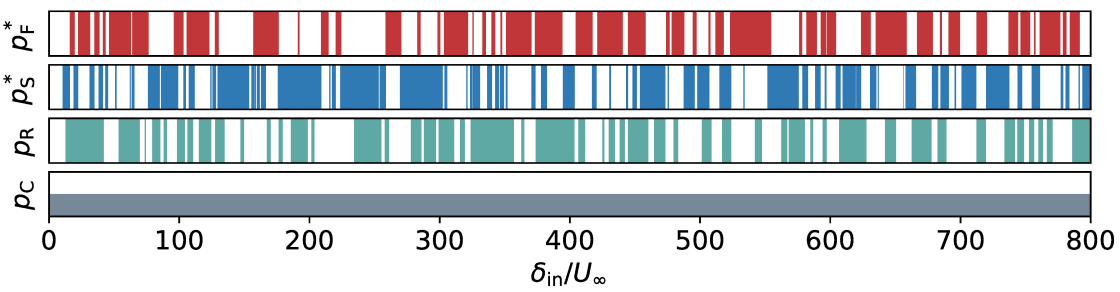

FIG. 10: Control inputs. p_F^*: optimal input for targeting fast LSMs; p_S^*: optimal input for targeting slow LSMs; p_R: random actuation; p_C: continuous actuation.

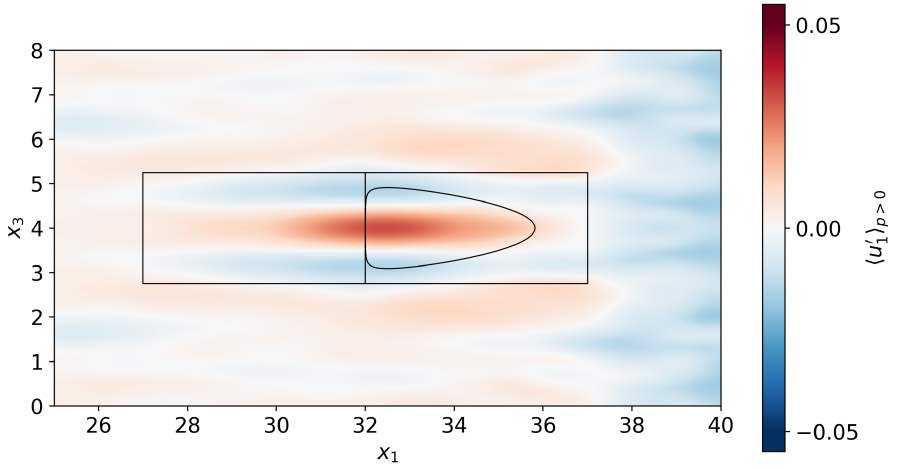

(a) $x_2 = 0.6\delta_{in}$.

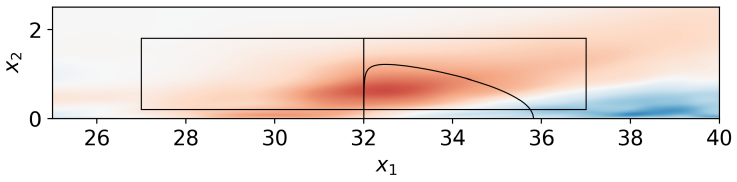

(b) $x_3 = 4\delta_{in}$.

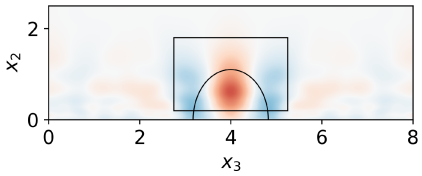

(c) $x_1 = 32\delta_{in}$.

FIG. 11: Conditionally-averaged velocity fluctuations u_1' for when $p_F^* > 0$.

area is less significant, compared to the other schemes. The picture is reversed when the jet is stronger than the baseline. While targeting fast LSMs leads to a smaller separation area (55.9% compared to 60.5% for the slow targets), the mean separation volume is higher than the random and continuous cases, as well as targeting slow LSMs.

C. Separation Volume and Area Distribution

The above metrics provide insight into how the actuation scheme alters the overall flow. However, since the jet is located in the center of the span of the domain, the localized effects can be obscured by the above "global" statistics. More information can be gained by looking at the distribution of the separation volume and area over the spanwise direction x_3. In particular, define

$$\frac{\mathrm{d}V}{\mathrm{d}x_3}(x_3) = \lim_{\delta x_3 \to 0} \frac{1}{\delta x_3} \int_0^{L_1} \int_0^{L_2} \int_{x_3 - \delta x_3/2}^{x_3 + \delta x_3/2} I(\tilde{u}_1 < 0)\, \mathrm{d}x_3\, \mathrm{d}x_2\, \mathrm{d}x_1 \tag{27}$$

and

$$\frac{\mathrm{d}A}{\mathrm{d}x_3}(x_3) = \lim_{\delta x_3 \to 0} \frac{1}{\delta x_3} \int_0^{L_1} \int_{x_3 - \delta x_3/2}^{x_3 + \delta x_3/2} I\left(\left. \frac{\partial \tilde{u}_1}{\partial y} \right|_{y=0} < 0 \right) \mathrm{d}x_3\, \mathrm{d}x_1 \tag{28}$$

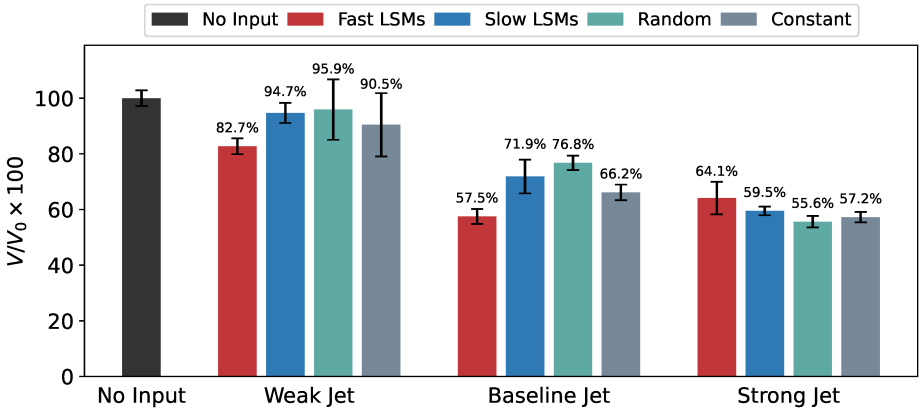

(a) Average separation volume, V.

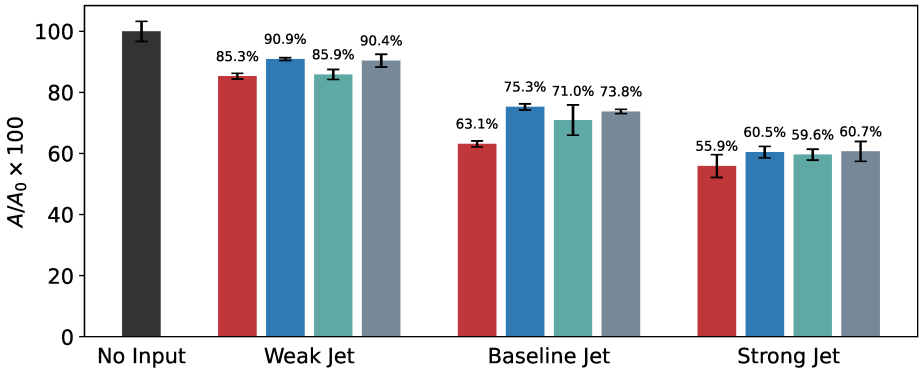

(b) Average separation area, A.

FIG. 12: Average separation volume and area, normalized by the mean values when no actuation occurs.

as the spanwise distribution of separated volume and area, respectively. In Fig. 13a, it can be seen that for the weak jet, the overall volume in the vicinity of the jet (between $x_3 = 2$ and $x_3 = 6$) is significantly smaller when targeting fast LSMs, compared to targeting slow LSMs. In fact, the performance of the random and continuous cases, which do not distinguish between fast and slow LSMs, falls between the fast and slow LSM targeting schemes. The same effect is noted over a wider span ($x_3 = 1$ to $x_3 = 7$) in the baseline case (Fig. 13b), which leads to more reattachment due to the increased jet strength. Further increase of the jet strength (Fig. 13c) leads to saturation, with the fast, random, and constant cases performing similarly between $x_3 = 1.5$ and $x_3 = 6.5$ and the slow case performing slightly worse in the same span.

A similar trend is observed by looking at the spanwise distribution of the reversed wall shear stress area in Fig. 14. Targeting fast LSMs leads to more reattachment near the center of the domain, compared to targeting slow LSMs, while the random and continuous cases fall between the fast and slow LSM targeting values. The difference is most notable in the baseline jet case, while in the strong jet case, reattachment performance is saturated, with the fast LSM targeting case performing marginally better.

The separation line on the wall for each case is presented in Fig. 15. In Figs. 15a and 15c, the separation lines are comparable. However, targeting fast LSMs tends to perform better in reducing the reattachment region, as shown in Fig. 12. In the baseline jet strength case, targeting fast LSMs notably outperforms the other two cases, leading to the center of the bubble reattaching almost completely. In contrast, targeting slow LSMs underperforms compared to the other three cases.

D. Momentum Distribution

In all cases, it can be observed that while the separation volume decreases near the center plane $x_3 = 4\delta_{\text{in}}$, the volume distribution tends to increase at the edges of the domain ($x_3 = 0\delta_{\text{in}}$ and $x_3 = 8\delta_{\text{in}}$). Since the boundary conditions at the sides are periodic, the simulations employed here represent an infinite array of actuators in the spanwise direction, spaced at $\Delta x_3 = 8\delta_{\text{in}}$. However, since the top boundary condition maintains a fixed u_2 velocity profile, there is only a limited amount of momentum that the jet force field can entrain from the free stream to increase near-wall momentum (in addition to the momentum increase due to the jet force field). This leads to a redistribution of momentum from the free stream and the sides of the domain ($x_3 \to 0$ and $x_3 \to 8$) to the center.

To better understand the momentum distribution within

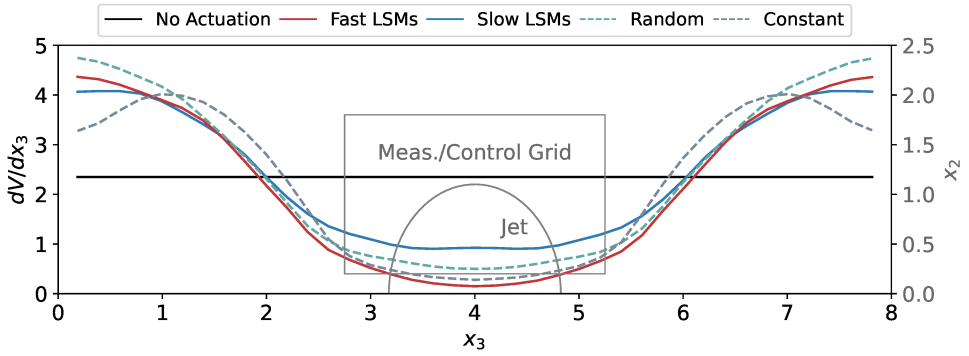

(a) Weak jet.

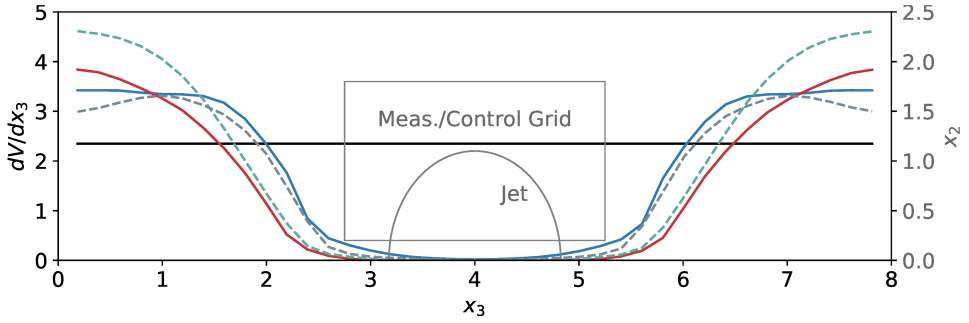

(b) Baseline jet.

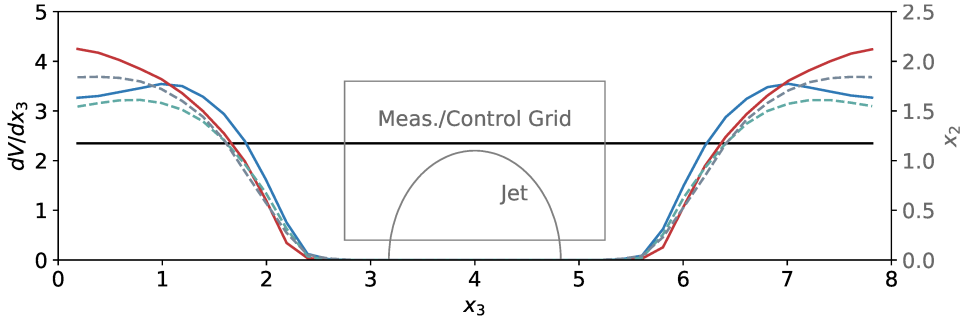

(c) Strong jet.

FIG. 13: Spanwise distribution of separation volume.

the domain, consider the spanwise momentum distribution around the separation bubble $35\delta_{\text{in}} \leq x_1 \leq 65$,

$$\frac{\mathrm{d}M_1}{\mathrm{d}x_3}(x_3) = \lim_{\delta x_3 \to 0} \frac{1}{\delta x_3} \int_{35\delta_{\text{in}}}^{65\delta_{\text{in}}} \int_0^{L_2} \int_{x_3-\delta x_3/2}^{x_3+\delta x_3/2} \rho \langle u_1(\mathbf{x}) \rangle \, \mathrm{d}x_3 \, \mathrm{d}x_2 \, \mathrm{d}x_1. \tag{29}$$

The above distribution for each case is given in Fig. 16. Computing the above distribution shows increased momentum at the center of the domain ($x_3 = 4\delta_{\text{in}}$), followed by a decrease of momentum below the no-actuation values at the sides of the domain, away from the jet, for all actuation cases. However, the total streamwise momentum in each case remains close to the no-actuation case, with a change of less than 0.1% of the area under the $\frac{\mathrm{d}M_1}{\mathrm{d}x_3}(x_3)$ curve for all cases.

In the baseline case and when targeting fast LSMs, the momentum at the center of the domain is notably lower than in the other actuation schemes (Fig. 16b). At the same time, it is more elevated away from the center plane and toward $x_3 = 1\delta_{\text{in}}$ and $x_3 = 7\delta_{\text{in}}$. A similar trend is observed in the strong jet case, with momentum lower at the center but better distributed toward the sides of the domain (Fig. 16c). The momentum distribution effects are less notable, however, in the weak jet case (Fig. 16a).

The momentum distribution can also be studied by examining the mean streamwise velocity $\langle u_1 \rangle$ at different $\mathbf{x}$ locations. In Fig. 17, $\langle u_1 \rangle$ velocity profiles on spanwise-normal planes are shown as $\langle u_1(x_2) \rangle$ line plots at various streamwise locations around the separation bubble. At the center of the domain ($x_3 = 4\delta_{\text{in}}$), the momentum away from the wall is decreased in the fast LSM targeting case relative to the slow LSM case. However, it increases near the wall further downstream, particularly in the favorable pressure gradient part of

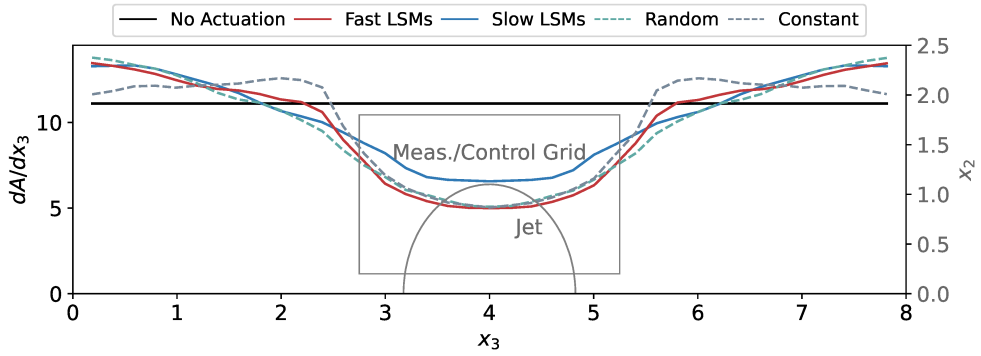

(a) Weak jet.

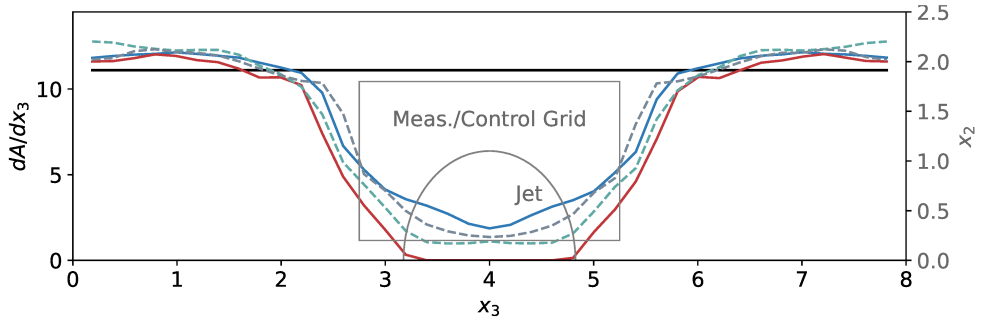

(b) Baseline jet.

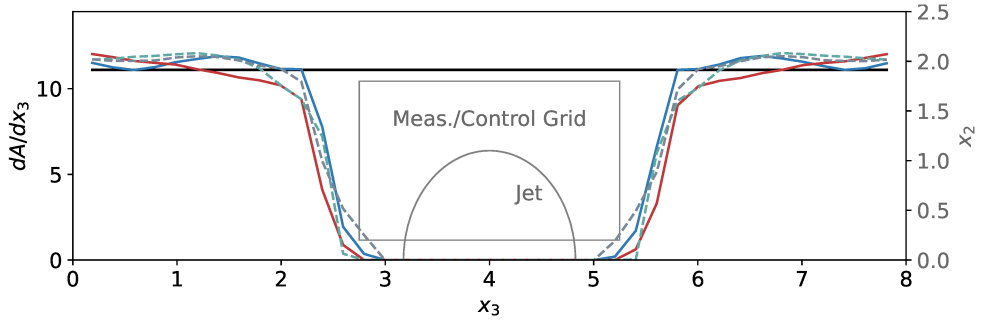

(c) Strong jet.

FIG. 14: Spanwise distribution of separation area.

the separation bubble ($x_1 > 50\delta_{in}$). Moving away from the center plane ($x_3 = 3\delta_{in}$ and $x_3 = 2\delta_{in}$), the mean velocity in the fast LSM targeting scheme tends to be higher than both the slow LSM and the no actuation cases closer to the wall. Further away from the center plane, however, $\langle u_1 \rangle$ is lower than the no actuation case for both the fast and slow LSM schemes due to the redistribution of momentum within the computational domain.

E. Instantaneous Flowfield

The streamwise velocity fluctuations, u_1', used to detect the LSMs are depicted in Fig. 18a as u_1' isosurfaces. Prior to the onset of the APG ($x_1 < 35$), long coherent structures with both high (red) and low (blue) streamwise momentum are visible. The size of these LSMs tends to increase substantially as the APG intensifies ($35 < x_1 < 50$), while they begin to break up in the FPG region ($50 < x_1 < 65$). Figure 18b shows the corresponding near-wall streamwise velocity, u_1, at $x_2 = 0.1\delta_{in}$ (which corresponds to $x_2^+ = 50$ at $x_1 = 32$, i.e., the beginning of the jet force field). The beginning of the APG, where the flow significantly slows down, resulting in the formation of the separation bubble (indicated by the $u_1 = 0$ isosurface between $x_1 = 40$ and $x_1 = 55$), is also visible. Both figures also indicate the location of the control setup.

F. Streamwise Voriticity

A simplified view of the benefit of targeting high-momentum large-scale motions (LSMs) for re-energizing a

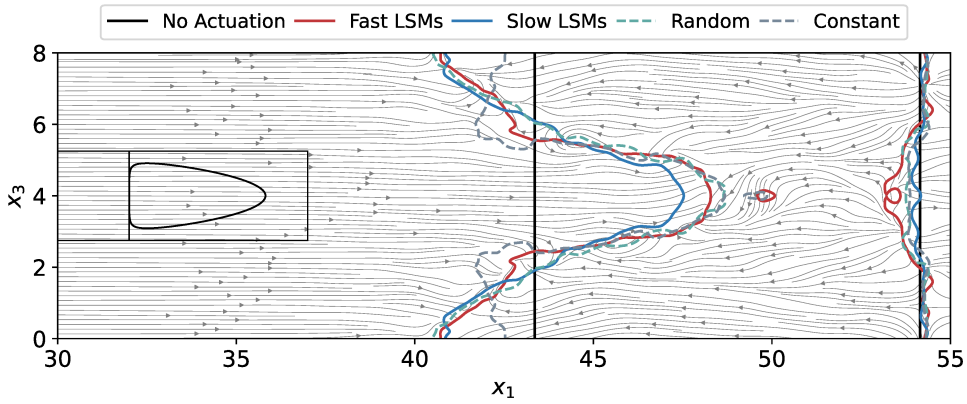

(a) Weak jet.

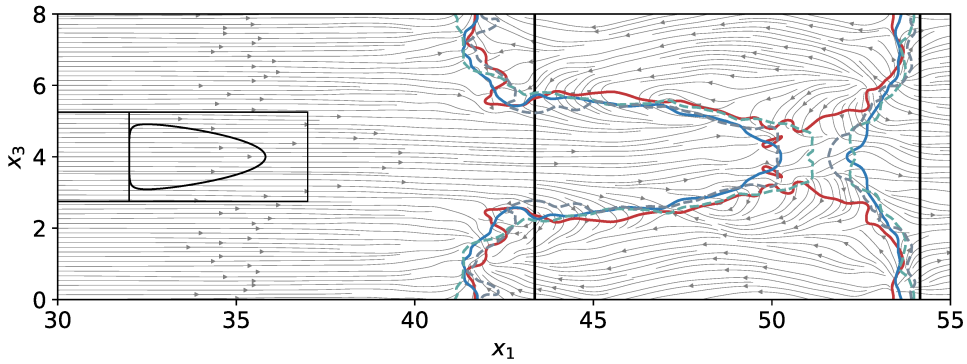

(b) Baseline jet.

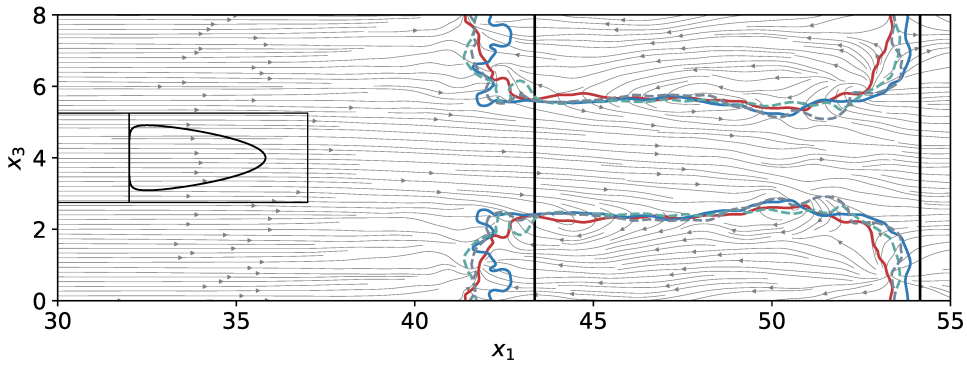

(c) Strong jet.

FIG. 15: Wall separation line ((x_1, x_3) at which $\partial u_1/\partial x_2 = 0$ at $x_2 = 0$). The streamlines correspond to the flow field of the fast LSMs case. The control setup is also visible for comparison.

turbulent boundary layer (TBL) and preventing separation is illustrated in Fig. 19. Slow-moving LSMs can be thought of as Q2 (or ejection) events, i.e., flow structures with $u_1' < 0$ and $u_2' > 0$, while fast-moving LSMs can be viewed as Q4 (or sweep) events, i.e., structures with $u_1' > 0$ and $u_2' < 0$[57]. These alternating low and high-momentum LSMs, which tend to be aligned with the flow direction, are accompanied by the formation of quasi-streamwise vortices, leading to the natural roll modes depicted in Fig. 19.

The natural roll mode in a turbulent boundary layer plays a significant role in the dynamics of the flow, as it contributes to the transfer of momentum between the wall and the bulk flow. Conceptually, pushing fast LSMs toward the wall should reinforce the intensity of the roll modes, leading to an increased exchange of momentum between the free stream and the near-wall flow. On the other hand, pushing slow-moving LSMs toward the wall should have the opposite effect, i.e., suppressing the natural roll modes. The increase in the intensity of mixing can be observed by looking at the root mean square (RMS) of the streamwise vorticity component ω_1 around the separation

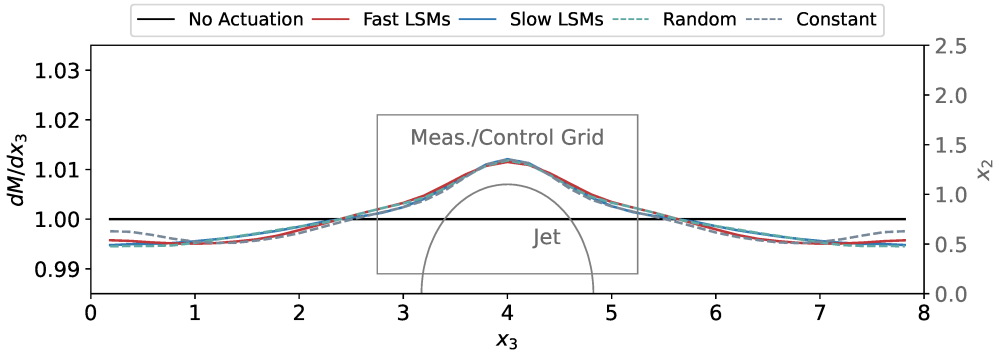

(a) Weak jet.

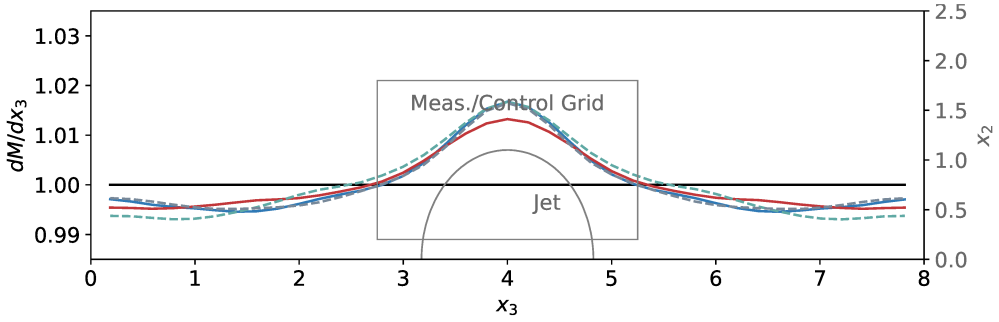

(b) Baseline jet.

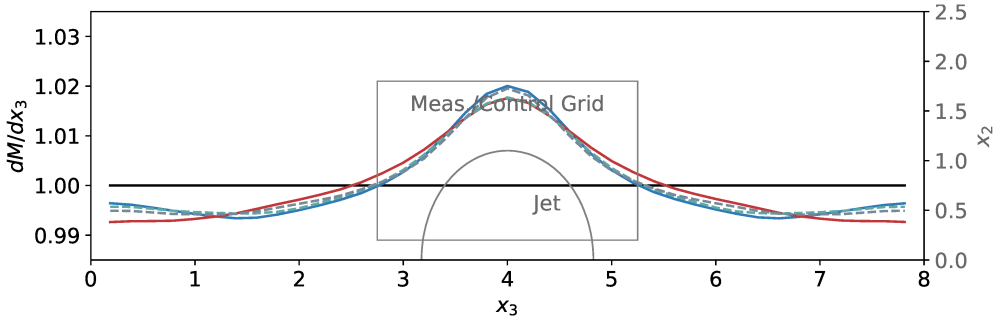

(c) Strong jet.

FIG. 16: Spanwise distribution of momentum.

bubble. In particular, consider

$$\frac{\mathrm{d}\omega_1}{\mathrm{d}x_3}(x_3) = \lim_{\delta x_3 \to 0} \frac{1}{\delta x_3} \int_{40\delta_{\mathrm{in}}}^{55\delta_{\mathrm{in}}} \int_{0}^{2\delta_{\mathrm{in}}} \int_{x_3-\delta x_3/2}^{x_3+\delta x_3/2} \langle \omega_1'(\mathbf{x})\omega_1'(\mathbf{x}) \rangle \, \mathrm{d}x_3 \, \mathrm{d}x_2 \, \mathrm{d}x_1 \tag{30}$$

The distribution for the baseline fast and slow LSM schemes can be observed in Fig. 20. Targeting fast LSMs results in a higher RMS value for ω_1 compared to targeting slow LSMs, with these elevated values prevailing throughout most of the domain's span. This finding supports the hypothesis that pushing fast LSMs toward the wall enhances mixing by amplifying the effect of the natural roll modes.

G. Discussion

The results presented here indicate that directing fast LSMs toward the wall can be beneficial for separation delay. It is important to recognize that the largest contribution to the reattachment of the flow is due to the momentum introduced by the jet itself. Irrespective of the targeting of LSMs, the actuator on its own can lead to a reduction in the separation area and volume. However, using the jet to direct fast LSMs toward the wall can lead to additional reattachment at no additional cost. This can be intuitively explained by the fact that when the jet is on and targets fast LSMs, the entrained flow will tend to have higher momentum than the average momentum of the turbulent boundary layer. In addition, as discussed in Subsection IV F, favoring fast LSMs can also increase the streamwise vorticity – and, therefore, mixing – in the flow,

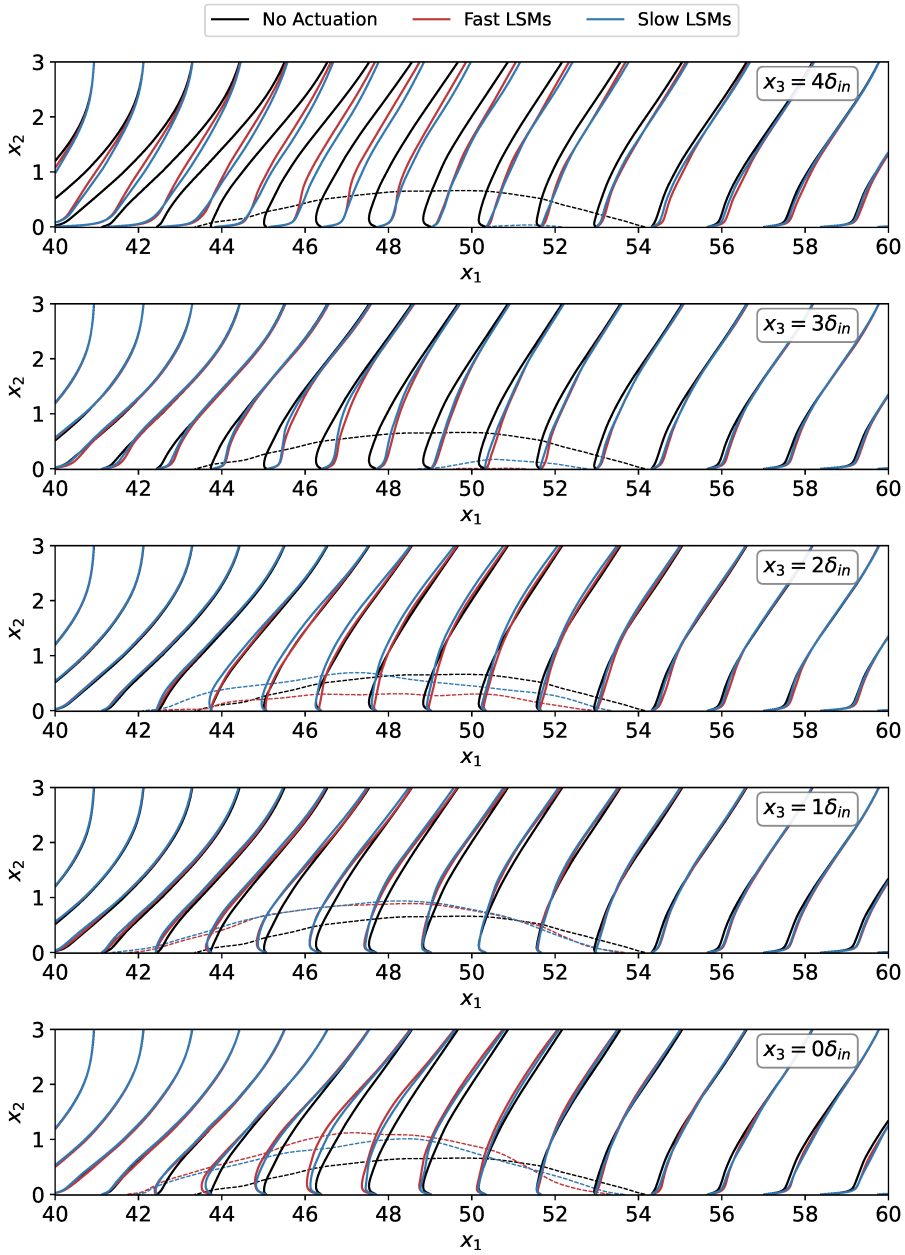

FIG. 17: Average streamwise velocity. The dashed lines indicate the location of the separation bubble, $u_1 = 0$, for each case.

due to the association of fast and slow LSMs with sweep and ejection events.

V. CONCLUSION

In this study, a model predictive control scheme was developed for targeting high-momentum LSMs in a turbulent boundary layer to delay separation. The proposed control strategy employs Taylor's hypothesis and reduced-order modeling within an optimal control framework, generating downwash at locations where fast LSMs are anticipated. A comprehensive comparison of targeting fast and slow LSMs, as well as random and continuous actuation schemes, highlighted the benefits of targeting fast LSMs for separation delay by enhancing momentum transfer from high to low momentum regions on the verge of separation.

The present study supports the idea that targeting fast LSMs has the potential to delay separation. However, to prove the above concept, several design choices had to be made that are, by no means, optimal. For instance, one could think of a control setup consisting of an array of smaller actuators that individually target narrower regions with fast LSMs, but collectively lead to a more even distribution of the separation delay in the spanwise direction instead of the effects being localized at the center of the domain, as seen in Fig. 15. Taylor's hy-

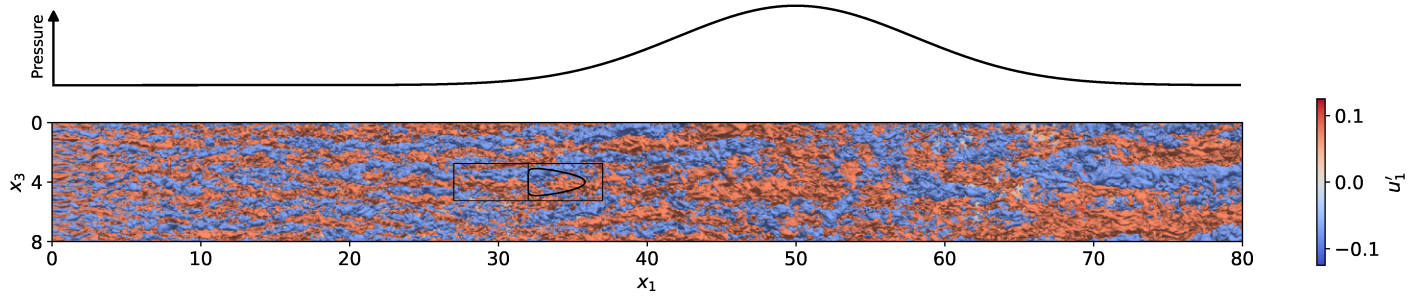

(a) Isosurfaces of $u_1' = \pm 0.075 U_\infty$.

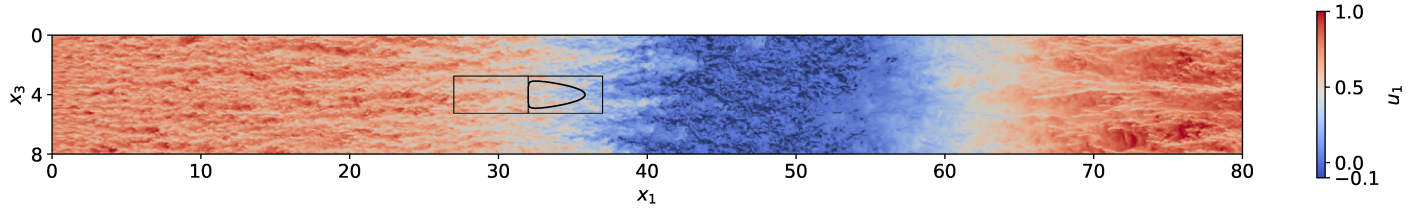

(b) Near-wall u_1 at $x_2 = 0.1\delta_{\text{in}}$. The instantaneous separation bubble is also visualized as an isosurface of $u_1' = 0$ (blue isosurface).

FIG. 18: Instantaneous view of LSMs.

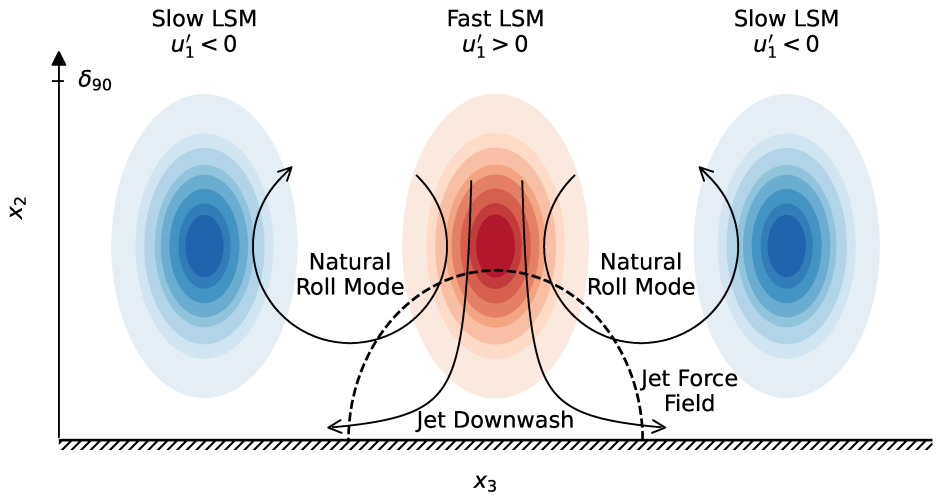

FIG. 19: Illustration of a streamwise-normal plane with alternating slow and fast LSMs. Pushing fast LSMs toward the wall has the potential to increase the intensity of streamwise vorticity and, thus, mixing.

pothesis for predicting the future location of LSMs could also be either improved by selecting a more appropriate convection velocity or replaced by a more sophisticated prediction model that also takes into account the deformation of an LSM by the effect of the jet, similar to Ref. 58.

This study is the first demonstration of the idea that LSMs can be selectively manipulated to achieve enhanced separation control in a turbulent boundary layer. There are many parameters, such as the detailed shape or pitch angle of the force field, that are not varied in this work but will be studied in subsequent work. The effect of the Reynolds number is also not explored in this study, but the broad idea is expected to hold and, perhaps, be even more effective at higher Reynolds numbers. This is because higher Reynolds numbers typically result in more energetic and larger turbulent structures[49,59], which can influence the dynamics of near-wall motions[60–62]

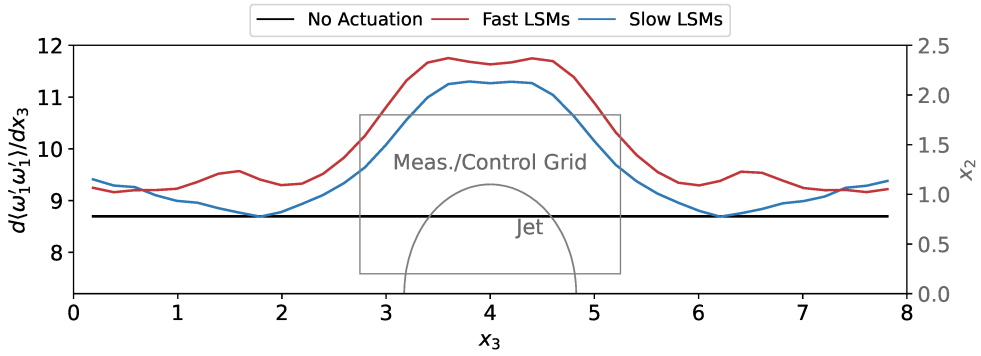

FIG. 20: Spanwise distribution of the streamwise vorticity RMS.

and are responsible for extreme wall shear events[63].

Further study of some of the design choices, such as the streamwise location of the actuator and the size and location of the measurement/control grids, have the potential to amplify the performance gains. Modeling choices, such as detecting LSMs from wall measurements and using more realistic actuators, instead of a body force field, can lead to more practical implementations of the proposed control scheme. Lastly, realistic geometries encountering adverse pressure gradients, such as airfoils, are a potential avenue for further research. Ongoing work at the Rensselaer Polytechnic Institute[64,65] is aimed at experimentally understanding and demonstrating the proposed control scheme and will be presented in the future.

ACKNOWLEDGMENTS

The authors would like to acknowledge support by NSF awards 2129494 and 2052811, as well as the Texas Advanced Computing Center (TACC) at The University of Texas at Austin for providing HPC resources. Alexandros Tsolovikos acknowledges support by the A. Onassis Foundation Scholarship.

DATA AVAILABILITY STATEMENT

The data that support the findings of this study are available from the corresponding author upon reasonable request.

Appendix A: Total Least-Squares Dynamic Mode Decomposition with Control

It is assumed that the high-dimensional dynamics of the system of interest have a discrete-time form of

$$\mathbf{y}(k+1) = \mathbf{f}(\mathbf{y}(k), \mathbf{p}(k), \mathbf{w}(k)), \tag{A1}$$

where $\mathbf{y} \in \mathbb{R}^{n_y}$ is the state (here, u_2' in the control box), $\mathbf{p} \in \mathbb{R}^{n_p}$ the control input, $\mathbf{w} \in \mathbb{R}^{n_w}$ the independent and identically distributed Gaussian white noise, and $\mathbf{f}(\cdot)$ the nonlinear operator that propagates the state $\mathbf{y}(k)$ by one time step.

The goal of tlsDMDc is to identify a linear reduced-order model of the underlying dynamics when (A1) is unknown or prohibitively expensive to compute in real-time, and only a limited number of noisy experimental or numerical data is available, as is typical in fluid dynamics applications.

In particular, given a set of $m+1$ ensemble-averaged snapshots of the velocity field $\mathbf{y}(k)$, $k = 0, \ldots, m$ generated from a sequence of inputs $p(k)$, $k = 0, \ldots, m-1$, the data can be arranged as

$$Y = \begin{bmatrix} \mathbf{y}(0) & \cdots & \mathbf{y}(m-1) \end{bmatrix} \in \mathbb{R}^{n_y \times m}, \tag{A2a}$$

$$Y' = \begin{bmatrix} \mathbf{y}(1) & \cdots & \mathbf{y}(m) \end{bmatrix} \in \mathbb{R}^{n_y \times m}, \tag{A2b}$$

$$P = \begin{bmatrix} \mathbf{p}(0) & \cdots & \mathbf{p}(m-1) \end{bmatrix} \in \mathbb{R}^{n_p \times m}. \tag{A2c}$$

A common way to reduce the dimensionality of the data when $n_y \gg 1$ is to project the high-dimensional state $\mathbf{y}(k)$ onto the proper orthogonal decomposition (POD) modes given by the singular value decomposition (SVD) of the data matrix

$$Y = U \Sigma V^{\mathrm{T}},$$

where the columns of matrix $U \in \mathbb{R}^{n_y \times m}$ are the orthonormal eigenvectors of YY^{T} or POD modes arranged by their energy content, i.e. their singular value, the columns of $V \in \mathbb{R}^{m \times m}$ are the orthonormal eigenvectors of $Y^{\mathrm{T}}Y$, and $\Sigma \in \mathbb{R}^{m \times m}$ is the diagonal matrix containing the singular values of Y arranged by their magnitude.

Projecting the high-dimensional snapshots $\mathbf{y}(k)$ on the range space of the matrix $U_{POD} \in \mathbb{R}^{n_y \times n_z}$ formed by the first (most energetic) n_z POD modes corresponding to the n_z largest singular values of Y is a common choice in model reduction methods that focuses the modeling efforts on the most important modes of the high-dimensional system while ignoring the least energetic (and, typically, noisy) ones. The high-dimensional state can then be approximated as

$$\mathbf{y}(k) \approx U_{POD} \mathbf{z}(k), \tag{A3}$$

where $\mathbf{z}(k) \in \mathbb{R}^{n_z}$ is the amplitude vector of the POD modes at time step k. In general, $\mathbf{z}(k)$ is approximated in a least-squares sense as $\mathbf{z}(k) = U_{POD}^{\mathrm{T}} \mathbf{y}(k)$. The snapshot matrices in

Eqs. (A2a) - (A2b) are also reduced as

$$Z = U_{POD}^{\mathrm{T}} Y, \quad Z' = U_{POD}^{\mathrm{T}} Y',$$

where Z, Z' are the POD mode amplitude matrices for the training data in Eqs. (A2a) and (A2b).

Like DMDc[53], it is assumed that the dynamics of the high-dimensional system are linear. Hence, the POD mode amplitudes $\mathbf{z}(k)$ also follow a linear state-space model, as the POD projection is linear. The reduced-order model has the form

$$\mathbf{z}(k+1) = A\mathbf{z}(k) + B\mathbf{p}(k) + \mathbf{e}(\mathbf{z}(k), \mathbf{p}(k), \mathbf{w}(k)), \tag{A4}$$

where $A \in \mathbb{R}^{n_z \times n_z}$ and $B \in \mathbb{R}^{n_z \times n_p}$ are the state and control transition matrices and $\mathbf{e}(\cdot)$ represents the error from the unmodeled nonlinear dynamics and process noise.

Following Ref. 35, in order to account for the noise in the data, it is assumed that the snapshots (Eqs. (A2a) and (A2b)) can be decomposed in a mean and noise part as

$$Y = \bar{Y} + E_Y, \quad Y' = \bar{Y}' + E_{Y'}$$

where $\bar{Y}$, $\bar{Y}'$ are the mean snapshots and E_Y, $E_{Y'}$ are the noise terms. After projection on the POD modes, the reduced-order snapshots become

$$Z = \bar{Z} + E_Z, \quad Z' = \bar{Z}' + E_{Z'}.$$

According to Ref. 35, the least-squares minimization approach typically used in DMD (and, consequently, DMDc) accounts only for the noise $E_{Z'}$ in the plus-one time step data Z', leading to a bias in the estimate of the dynamics that depends on E_Z. Alternatively, one can use total least-squares DMD to account for the noise in both Z and Z'. The approximation of the dynamics can be expressed as

$$\bar{Z}' + E_{Z'} = A(\bar{Z} + E_Z) + BP \tag{A5}$$

and the error in both components can be minimized simultaneously by solving the least-squares minimization problem

$$\min_{A,B} \quad \left\| \begin{bmatrix} E_Z & E_{Z'} \end{bmatrix} \right\|_F^2. \tag{A6}$$

Equation (A5) can be reformulated as

$$\begin{bmatrix} A & B & -I \end{bmatrix} \begin{bmatrix} \bar{Z} + E_Z \\ P \\ \bar{Z}' + E_Z' \end{bmatrix} = 0 \tag{A7}$$

and the solution to Eq. (A6) can be computed using the truncated SVD

$$\begin{bmatrix} \bar{Z} + E_Z \\ P \\ \bar{Z}' + E_Z' \end{bmatrix} = U \Sigma_{n_z+1} V^* = \begin{bmatrix} U_{11} & U_{12} \\ U_{21} & U_{22} \end{bmatrix} \begin{bmatrix} \Sigma_1 & 0 \\ 0 & 0 \end{bmatrix} \begin{bmatrix} V_1 \\ V_2 \end{bmatrix}$$

where only the first $n_z + 1$ singular values are kept, leading to an unbiased estimate of A and B

$$\begin{bmatrix} A & B \end{bmatrix} = U_{21} U_{11}^{-1}. \tag{A8}$$

The final outcome of tlsDMDc is a reduced-order state-space model of the form

$$\mathbf{z}(k+1) = A\mathbf{z}(k) + B\mathbf{p}(k) \tag{A9a}$$

$$\mathbf{y}(k) = C\mathbf{z}(k) \tag{A9b}$$

where $\mathbf{z}(k)$ is the reduced-order state, $\mathbf{p}(k)$ the control input, and $\mathbf{y}(k)$ the original, high-dimensional state (e.g., the flow-field), with $C = U_{POD}$.

Notice that in the above total least-squares optimization, only the noise in Z and Z' is minimized, since the control input matrix P is noise-free (e.g. a sequence of zeros and ones). The above is an extension of tlsDMD to systems with control inputs (tlsDMDc).

Appendix B: Formulating the Optimal Output Tracking Controller as a Semi-Definite Program

Since the reduced-order system of Eq. (A9) is time-invariant, without loss of generality, consider $t = 0$. The goal of the optimal tracking control problem is to find the sequence of inputs $\pi_0^* = \{p^*(0), \ldots, p^*(N-1)\}$ that solves the optimization problem (21).

Instead of minimizing the cost function of Problem (21), alternatively, one can minimize

$$J_1(\boldsymbol{\pi}) = \boldsymbol{\pi}^{\mathrm{T}} \mathbf{R} \boldsymbol{\pi} + \boldsymbol{\upsilon}^{\mathrm{T}} \mathbf{Q} \boldsymbol{\upsilon} - 2\boldsymbol{\upsilon}^{\mathrm{T}} \boldsymbol{\phi} \tag{B1}$$

where

$$\boldsymbol{\pi} := \begin{bmatrix} p(0) \\ \vdots \\ p(N-1) \end{bmatrix}, \quad \boldsymbol{\upsilon} := \begin{bmatrix} \mathbf{y}(1) \\ \vdots \\ \mathbf{y}(N) \end{bmatrix}, \quad \boldsymbol{\phi} := \begin{bmatrix} Q\mathbf{y}_{des}(1) \\ \vdots \\ Q\mathbf{y}_{des}(N) \end{bmatrix},$$

$$\mathbf{R} := \mathrm{bdiag}\{R, \ldots, R\}, \quad \mathbf{Q} := \mathrm{bdiag}\{Q, \ldots, Q\},$$

and $\mathrm{bdiag}\{A_1, \ldots, A_p\}$ denotes the block diagonal matrix with the matrices A_i as its diagonal blocks.

From Eqs. (A9a) and (A9b), and with initial condition $\mathbf{z}(0) = \mathbf{z}_0$, the sequence of outputs can be written as

$$\begin{aligned}
\mathbf{y}(1) &= C\mathbf{z}(1) \\
&= CA\mathbf{z}_0 + Cp(0) \\
\mathbf{y}(2) &= C\mathbf{z}(2) \\
&= CA^2\mathbf{z}_0 + CABp(0) + CBp(1) \\
&\vdots \\
\mathbf{y}(N) &= C\mathbf{z}(N) \\
&= CA^N\mathbf{z}_0 + CA^{N-1}Bp(0) + \cdots + CBp(N-1)
\end{aligned}$$

or, more compactly, as

$$\boldsymbol{\upsilon} = \boldsymbol{\Omega}\mathbf{z}_0 + \boldsymbol{\Gamma}\boldsymbol{\pi}, \tag{B2}$$

with $\boldsymbol{\Omega}, \boldsymbol{\Gamma}$ defined as

$$\boldsymbol{\Omega} := \begin{bmatrix} CA \\ \vdots \\ CA^N \end{bmatrix}, \quad \boldsymbol{\Gamma} := \begin{bmatrix} CB & \cdots & 0 \\ \vdots & \ddots & 0 \\ CA^{N-1}B & \cdots & CB \end{bmatrix}.$$

Eq. (B2) can now be used to replace $\boldsymbol{v}$ in Eq. (B1) and derive a cost function that depends only on the input vector $\boldsymbol{\pi}$,

$$J(\boldsymbol{\pi}) = \boldsymbol{\pi}^{\mathrm{T}}\left[\boldsymbol{\Gamma}^{\mathrm{T}}\mathbf{Q}\boldsymbol{\Gamma} + \mathbf{R}\right]\boldsymbol{\pi} + 2\boldsymbol{\pi}^{\mathrm{T}}\boldsymbol{\Gamma}^{\mathrm{T}}\left(\mathbf{Q}\boldsymbol{\Omega}\mathbf{z}_0 - \boldsymbol{\phi}\right), \tag{B3}$$

where the factors that are independent of $\boldsymbol{\pi}$ have been omitted.

The output tracking problem with input constraints can now be expressed as the following unconstrained **binary quadratic program** (BQP):

$$\begin{aligned} \underset{\boldsymbol{\pi}}{\text{minimize}} \quad & \boldsymbol{\pi}^{\mathrm{T}} H \boldsymbol{\pi} + \boldsymbol{\pi}^{\mathrm{T}} f \\ \text{subject to} \quad & \boldsymbol{\pi} \in \{0,\ 1\}^N \end{aligned} \tag{B4}$$

where

$$H = \boldsymbol{\Gamma}^{\mathrm{T}}\mathbf{Q}\boldsymbol{\Gamma} + \mathbf{R}, \quad f = 2\boldsymbol{\Gamma}^{\mathrm{T}}\left(\mathbf{Q}\boldsymbol{\Omega}\mathbf{z}_0 - \boldsymbol{\phi}\right).$$

The problem of solving a BQP like (B4) is known to be NP-hard[55], meaning it is computationally difficult to find an optimal solution. However, various optimization algorithms and heuristics have been developed to solve BQPs, including branch and bound, simulated annealing, genetic algorithms, and semi-definite programming[66].

If $\boldsymbol{\pi} \in \mathbb{R}^N$, then problem (B4) can be relaxed to a quadratically constrained quadratic program (QCQP) with the addition of the constraint $p(k) = p^2(k)$, or

$$\begin{aligned} \underset{\boldsymbol{\pi}}{\text{minimize}} \quad & \boldsymbol{\pi}^{\mathrm{T}} H \boldsymbol{\pi} + \boldsymbol{\pi}^{\mathrm{T}} f \\ \text{subject to} \quad & \boldsymbol{\pi} = \mathrm{diag}(\boldsymbol{\pi}\boldsymbol{\pi}^{\mathrm{T}}). \end{aligned} \tag{B5}$$

If $\boldsymbol{\Pi} = \boldsymbol{\pi}\boldsymbol{\pi}^{\mathrm{T}}$, further relaxation to a semi-definite program of the form

$$\begin{aligned} \underset{\boldsymbol{\pi}}{\text{minimize}} \quad & \mathrm{trace}\left(H\boldsymbol{\Pi}\right) + \boldsymbol{\pi}^{\mathrm{T}} f \\ \text{subject to} \quad & \boldsymbol{\pi} = \mathrm{diag}(\boldsymbol{\Pi}) \\ & \begin{pmatrix} 1 & \boldsymbol{\pi}^{\mathrm{T}} \\ \boldsymbol{\pi} & \boldsymbol{\Pi} \end{pmatrix} \succcurlyeq 0. \end{aligned} \tag{B6}$$

can be achieved using the Schur complement. The above problem can then be solved efficiently using, for instance, interior point methods.

[1] A. Townsend, *The structure of turbulent shear flow* (Cambridge university press, 1980).

[2] S. K. Robinson, "Coherent motions in the turbulent boundary layer," Annual Review of Fluid Mechanics **23**, 601–639 (1991).

[3] R. J. Adrian, C. D. Meinhart, and C. D. Tomkins, "Vortex organization in the outer region of the turbulent boundary layer," Journal of fluid Mechanics **422**, 1–54 (2000).

[4] B. Balakumar and R. Adrian, "Large-and very-large-scale motions in channel and boundary-layer flows," Philosophical Transactions of the Royal Society A: Mathematical, Physical and Engineering Sciences **365**, 665–681 (2007).

[5] N. Hutchins and I. Marusic, "Evidence of very long meandering features in the logarithmic region of turbulent boundary layers," Journal of Fluid Mechanics **579**, 1–28 (2007).

[6] K. Kim and R. Adrian, "Very large-scale motion in the outer layer," Physics of Fluids **11**, 417–422 (1999).

[7] M. Guala, S. Hommema, and R. Adrian, "Large-scale and very-large-scale motions in turbulent pipe flow," Journal of Fluid Mechanics **554**, 521 (2006).

[8] J. C. Del Alamo, J. Jiménez, P. Zandonade, and R. D. Moser, "Scaling of the energy spectra of turbulent channels," Journal of Fluid Mechanics **500**, 135–144 (2004).

[9] J. Lee, J. H. Lee, J.-I. Choi, and H. J. Sung, "Spatial organization of large- and very-large-scale motions in a turbulent channel flow," Journal of fluid mechanics **749**, 818–840 (2014).

[10] R. J. Adrian, "Hairpin vortex organization in wall turbulence," Physics of Fluids **19**, 041301 (2007).

[11] P.-Å. Krogstad and P. E. Skåre, "Influence of a strong adverse pressure gradient on the turbulent structure in a boundary layer," Physics of Fluids **7**, 2014–2024 (1995).

[12] Z. Harun, J. P. Monty, R. Mathis, and I. Marusic, "Pressure gradient effects on the large-scale structure of turbulent boundary layers," Journal of Fluid Mechanics **715**, 477–498 (2013).

[13] J.-H. Lee and H. J. Sung, "Structures in turbulent boundary layers subjected to adverse pressure gradients," Journal of fluid mechanics **639**, 101–131 (2009).

[14] S. Rahgozar and Y. Maciel, "Low-and high-speed structures in the outer region of an adverse-pressure-gradient turbulent boundary layer," Experimental thermal and fluid science **35**, 1575–1587 (2011).

[15] J. H. Lee, "Large-scale motions in turbulent boundary layers subjected to adverse pressure gradients," Journal of Fluid Mechanics **810**, 323–361 (2017).

[16] P. Moin and T. Bewley, "Feedback control of turbulence," (1994).

[17] M. Gad-el Hak, *Flow Control: Passive, Active, and Reactive Flow Management* (Cambridge University Press, 2000).

[18] R. Rathnasingham and K. S. Breuer, "Active control of turbulent boundary layers," Journal of Fluid Mechanics **495**, 209–233 (2003).

[19] G. Karniadakis and K.-S. Choi, "Mechanisms on transverse motions in turbulent wall flows," Annual review of fluid mechanics **35**, 45–62 (2003).

[20] I. Marusic, K. Talluru, and N. Hutchins, "Controlling the large-scale motions in a turbulent boundary layer," in *Fluid-structure-sound interactions and control* (Springer, 2014) pp. 17–26.

[21] M. Abbassi, W. Baars, N. Hutchins, and I. Marusic, "Skin-friction drag reduction in a high-Reynolds-number turbulent boundary layer via real-time control of large-scale structures," International Journal of Heat and Fluid Flow **67**, 30–41 (2017).

[22] A. Tsolovikos, S. Suryanarayanan, E. Bakolas, and D. Goldstein, "Model predictive control of material volumes with application to vortical structures," AIAA Journal **59**, 4057–4070 (2021).

[23] A. Tsolovikos, A. Jariwala, S. Suryanarayanan, E. Bakolas, and D. Goldstein, "Separation delay in turbulent boundary layers via model predictive control of large-scale motions," Bulletin of the American Physical Society (2022).

[24] A. Jariwala, A. Tsolovikos, S. Suryanarayanan, D. B. Goldstein, and E. Bakolas, "On the effect of manipulating large scale motions in a boundary layer," in *AIAA AVIATION 2022 Forum* (2022) p. 3771.

[25] M. Ja'fari, A. J. Jaworski, and A. Rona, "Numerical study of flow separation control over a circular hump using synthetic jet actuators," AIP Advances **12** (2022).

[26] X. Geng, Z. Sun, Z. Li, Z. Shi, K. Cheng, and B. Khoo, "Effect of flow structure frequency on flow separation control using dielectric barrier discharge actuator," Physics of Fluids **34** (2022).

[27] C. S. Vila and O. Flores, "Wall-based identification of coherent structures in wall-bounded turbulence," in *Journal of Physics: Conference Series*, Vol. 1001 (IOP Publishing, 2018) p. 012007.

[28] R. J. Pabon, L. Ukeiley, M. Sheplak, and C. B. Keane, "Characteristics of turbulent boundary layer large scale motions using direct fluctuating wall shear stress measurements," Physical Review Fluids **3**, 114604 (2018).

[29] A. Güemes, S. Discetti, and A. Ianiro, "Sensing the turbulent large-scale motions with their wall signature," Physics of Fluids **31**, 125112 (2019).

[30] T. Brauner, S. Laizet, N. Benard, and E. Moreau, "Modelling of dielectric barrier discharge plasma actuators for direct numerical simulations," in *8th AIAA Flow Control Conference* (2016) p. 3774.

[31] S. Gildersleeve and M. Amitay, "Three-dimensional wake characteristics associated with the jet assisted surface mounted actuator," in *2018 Flow Control Conference* (2018) p. 3060.

[32] G. I. Taylor, "The spectrum of turbulence," Proceedings of the Royal Society of London. Series A-Mathematical and Physical Sciences **164**, 476–490 (1938).

[33]D. J. Dennis and T. B. Nickels, "On the limitations of Taylor's hypothesis in constructing long structures in a turbulent boundary layer," Journal of Fluid Mechanics **614**, 197–206 (2008).
[34]J. C. Del Alamo and J. Jiménez, "Estimation of turbulent convection velocities and corrections to Taylor's approximation," Journal of Fluid Mechanics **640**, 5–26 (2009).
[35]S. Dawson, M. S. Hemati, M. O. Williams, and C. W. Rowley, "Characterizing and correcting for the effect of sensor noise in the dynamic mode decomposition," Exp. in Fluids **57**, 1–19 (2016).
[36]A. T. Patera, "A spectral element method for fluid dynamics: laminar flow in a channel expansion," Journal of computational Physics **54**, 468–488 (1984).
[37]J. W. L. Paul F. Fischer and S. G. Kerkemeier, "Nek5000 web page," (2008), http://nek5000.mcs.anl.gov.
[38]P. Schlatter, S. Stolz, and L. Kleiser, "LES of transitional flows using the approximate deconvolution model," International journal of heat and fluid flow **25**, 549–558 (2004).
[39]A. Bobke, R. Vinuesa, R. Örlü, and P. Schlatter, "History effects and near equilibrium in adverse-pressure-gradient turbulent boundary layers," Journal of Fluid Mechanics **820**, 667–692 (2017).
[40]"Turbulent boundary layers around wing sections up to Rec= 1,000,000, author=Vinuesa, Ricardo and Negi, Prabal Singh and Atzori, M and Hanifi, Ardeshir and Henningson, Dan S and Schlatter, Philipp, journal=International Journal of Heat and Fluid Flow, volume=72, pages=86–99, year=2018, publisher=Elsevier," .
[41]P. Schlatter and R. Örlü, "Turbulent boundary layers at moderate Reynolds numbers: inflow length and tripping effects," Journal of Fluid Mechanics **710**, 5–34 (2012).
[42]T. S. Lund, X. Wu, and K. D. Squires, "Generation of turbulent inflow data for spatially-developing boundary layer simulations," Journal of computational physics **140**, 233–258 (1998).
[43]M. L. Shur, P. R. Spalart, M. K. Strelets, and A. K. Travin, "Synthetic turbulence generators for RANS-LES interfaces in zonal simulations of aerodynamic and aeroacoustic problems," Flow, turbulence and combustion **93**, 63–92 (2014).
[44]J. Jiménez, S. Hoyas, M. P. Simens, and Y. Mizuno, "Turbulent boundary layers and channels at moderate Reynolds numbers," Journal of Fluid Mechanics **657**, 335–360 (2010).
[45]Y. Na and P. Moin, "Direct numerical simulation of a separated turbulent boundary layer," Journal of Fluid Mechanics **374**, 379–405 (1998).
[46]G. Coleman, C. Rumsey, and P. Spalart, "Numerical study of turbulent separation bubbles with varying pressure gradient and Reynolds number," Journal of Fluid Mechanics **847**, 28–70 (2018).
[47]J.-L. Aider, J.-F. Beaudoin, and J. E. Wesfreid, "Drag and lift reduction of a 3D bluff-body using active vortex generators," Experiments in fluids **48**, 771–789 (2010).
[48]T. C. Corke, C. L. Enloe, and S. P. Wilkinson, "Dielectric barrier discharge plasma actuators for flow control," Annual review of fluid mechanics **42**, 505–529 (2010).
[49]J. H. Lee and H. J. Sung, "Very-large-scale motions in a turbulent boundary layer," Journal of Fluid Mechanics **673**, 80 (2011).
[50]C. Atkinson, N. A. Buchmann, and J. Soria, "An experimental investigation of turbulent convection velocities in a turbulent boundary layer," Flow, Turbulence and Combustion **94**, 79–95 (2015).
[51]C. W. Rowley, I. Mezić, S. Bagheri, P. Schlatter, and D. S. Henningson, "Spectral analysis of nonlinear flows," Journal of fluid mechanics **641**, 115–127 (2009).
[52]P. J. Schmid, "Dynamic mode decomposition of numerical and experimental data," Journal of fluid mechanics **656**, 5–28 (2010).
[53]J. L. Proctor, S. L. Brunton, and J. N. Kutz, "Dynamic mode decomposition with control," SIAM Journal on Applied Dynamical Systems **15**, 142–161 (2016).
[54]M. S. Hemati, C. W. Rowley, E. A. Deem, and L. N. Cattafesta, "Debiasing the dynamic mode decomposition for applied Koopman spectral analysis of noisy datasets," Theoretical and Computational Fluid Dynamics **31**, 349–368 (2017).
[55]J. Park and S. Boyd, "A semidefinite programming method for integer convex quadratic minimization," Optimization Letters **12**, 499–518 (2018).
[56]P. Welch, "The use of fast Fourier transform for the estimation of power spectra: a method based on time averaging over short, modified periodograms," IEEE Transactions on audio and electroacoustics **15**, 70–73 (1967).
[57]J. M. Wallace, "Quadrant analysis in turbulence research: history and evolution," Annual Review of Fluid Mechanics **48**, 131–158 (2016).
[58]A. Tsolovikos, S. Suryanarayanan, E. Bakolas, and D. B. Goldstein, "Toward model-based control of near-wall turbulent coherent structures," in *AIAA Scitech 2020 Forum* (2020) p. 1319.
[59]A. J. Smits, B. J. McKeon, and I. Marusic, "High–Reynolds number wall turbulence," Annual Review of Fluid Mechanics **43** (2011), 10.1146/annurev-fluid-122109-160753.
[60]R. Mathis, N. Hutchins, and I. Marusic, "Large-scale amplitude modulation of the small-scale structures in turbulent boundary layers," Journal of Fluid Mechanics **628**, 311–337 (2009).
[61]N. Hutchins and I. Marusic, "Large-scale influences in near-wall turbulence," Philosophical Transactions of the Royal Society A: Mathematical, Physical and Engineering Sciences **365**, 647–664 (2007).
[62]I. Marusic, R. Mathis, and N. Hutchins, "High Reynolds number effects in wall turbulence," International Journal of Heat and Fluid Flow **31**, 418–428 (2010).
[63]C. Pan and Y. Kwon, "Extremely high wall-shear stress events in a turbulent boundary layer," in *Journal of Physics: Conference Series*, Vol. 1001 (IOP Publishing, 2018) p. 012004.
[64]J. Wylie and M. Amitay, "Experimental generation of large-scale motion for boundary layer control," Bulletin of the American Physical Society (2022).
[65]J. Wylie, A. Jariwala, S. Suryanarayanan, D. Goldstein, and M. Amitay, "Hairpin vortex generation for physio-cyber simulations and control," Bulletin of the American Physical Society (2023).
[66]G. Kochenberger, J.-K. Hao, F. Glover, M. Lewis, Z. Lü, H. Wang, and Y. Wang, "The unconstrained binary quadratic programming problem: a survey," Journal of combinatorial optimization **28**, 58–81 (2014).